Opto-Electronic Advances

ISSN 2096-4579 CN 51-1781/TN

# Terahertz technology in intraoperative neurodiagnostics: A review

Nikita V. Chernomyrdin, Guzel R. Musina, Pavel V. Nikitin, Irina N. Dolganova, Anna S. Kucheryavenko, Anna I. Alekseeva, Yuye Wang, Degang Xu, Qiwu Shi, Valery V. Tuchin and Kirill I. Zaytsev

**Citation:** Chernomyrdin NV, Musina GR, Nikitin PV, Dolganova IN, Kucheryavenko AS et al. Terahertz technology in intraoperative neurodiagnostics: A review. *Opto-Electron Adv* **6**, 220071(2023).

https://doi.org/10.29026/oea.2023.220071

Received: 19 April 2022; Accepted: 4 June 2022; Published online: 29 November 2022

Opto-Electronic Advances

Review

May 2023, Vol. 6, No. 5

DOI: 10.29026/oea.2023.220071

# Terahertz technology in intraoperative neurodiagnostics: A review

Nikita V. Chernomyrdin[1,2]*, Guzel R. Musina[1], Pavel V. Nikitin[3], Irina N. Dolganova[2,4], Anna S. Kucheryavenko[1,4], Anna I. Alekseeva[3,5], Yuye Wang[6], Degang Xu[6], Qiwu Shi[7], Valery V. Tuchin[8,9]* and Kirill I. Zaytsev[1,2]*

Terahertz (THz) technology offers novel opportunities in biology and medicine, thanks to the unique features of THz-wave interactions with tissues and cells. Among them, we particularly notice strong sensitivity of THz waves to the tissue water, as a medium for biochemical reactions and a main endogenous marker for THz spectroscopy and imaging. Tissues of the brain have an exceptionally high content of water. This factor, along with the features of the structural organization and biochemistry of neuronal and glial tissues, makes the brain an exciting subject to study in the THz range. In this paper, progress and prospects of THz technology in neurodiagnostics are overviewed, including diagnosis of neurodegenerative disease, myelin deficit, tumors of the central nervous system (with an emphasis on brain gliomas), and traumatic brain injuries. Fundamental and applied challenges in study of the THz-wave – brain tissue interactions and development of the THz biomedical tools and systems for neurodiagnostics are discussed.

**Keywords:** THz technology; THz spectroscopy and imaging; superresolution imaging; biophotonics; brain; neurodiagnosis; tumor; glioma; neurodegenerative diseases; brain injury; light scattering

Chernomyrdin NV, Musina GR, Nikitin PV, Dolganova IN, Kucheryavenko AS et al. Terahertz technology in intraoperative neurodiagnostics: A review. *Opto-Electron Adv* **6**, 220071 (2023).

## Introduction

Terahertz (THz) spectral range is situated between the infrared (IR) and microwave bands and spans the frequencies of ~0.1–3.0 THz, or the wavelengths of ~3 mm–100 μm[1]. Advancement in THz spectroscopy and imaging is driven by a rapid progress in femtosecond laser technologies and novel efficient approaches for the THz-wave generation and detection[2–7]. Since the first experimental observation of THz heat rays by Rubens and Nichols[8], THz technology offers a variety of applications in fundamental and applied physics. Auston's research on photoconductivity in semiconductor, excited by the visible / near-IR femtosecond laser pulses, leads to the development of pulsed THz photoconductive antenna-emitters

[1]Prokhorov General Physics Institute of the Russian Academy of Sciences, Moscow 119991, Russia; [2]Bauman Moscow State Technical University, Moscow 105005, Russia; [3]Institute for Regenerative Medicine, Sechenov University, Moscow 119991, Russia; [4]Institute of Solid State Physics of the Russian Academy of Sciences, Chernogolovka 142432, Russia; [5]Research Institute of Human Morphology, Moscow 117418, Russia; [6]School of Precision Instrument and Optoelectronic Engineering, Tianjin University, Tianjin 300000, China; [7]College of Materials Science and Engineering, Sichuan University, Chengdu 610000, China; [8]Science Medical Center, Saratov State University, Saratov 410012, Russia; [9]Institute of Precision Mechanics and Control, FRC "Saratov Scientific Centre of the Russian Academy of Sciences", Saratov 410028, Russia.
*Correspondence: NV Chernomyrdin, E-mail: chernik-a@yandex.ru; VV Tuchin, E-mail: tuchinvv@mail.ru; KI Zaytsev, E-mail: kirzay@gmail.com
Received: 19 April 2022; Accepted: 4 June 2022; Published online: 29 November 2022

and detectors, related opto-electronic components and principles of THz-wave generation and detection, THz pulsed spectroscopy (TPS) and THz pulsed imaging (TPI) systems at the turn of the XX and XXI centuries[3,4,9]. Principles of THz pulsed spectroscopy and imaging allow one to develop quite portable, ergonomic, and cost-effective THz opto-electronic instruments for biomedical applications[10].

Nowadays, a considerable attention is paid to fundamental and applied research in the areas of early non-invasive, least-invasive and intraoperative THz diagnosis of malignant and benign neoplasms with different nosologies and localizations (such as the skin, mucosa, colon, breast, stomach, liver, etc.)[11–26], diabetes mellitus[27], tissue injuries[28], hydration[29], and viability[30]. Therapeutic applications of THz waves also attract considerable attentions, where both thermal and nonthermal exposure effects are observed, such as regulation of gene expression, biological membrane permeability, deoxyribonucleic acid (DNA) demethylation, etc.[31].

The versatility of THz technologies is due to the unique features of THz-radiation – tissue interactions, including the strong sensitivity of THz waves to the content and state of tissue water[17], that underlies the tissue biochemistry, largely determines the effective complex dielectric permittivity of hydrated tissues, and forms a highly sensitive endogenous marker for THz spectroscopy and imaging. For example, at the frequency of $\nu = 1.0$ THz, the refractive index and absorption coefficient of fibrous connective tissues, with the water content as high as $\approx$ 60%–75% (by volume), are $n \approx 1.95$ and $\alpha = 200$ cm$^{-1}$, respectively, which are significantly higher than those of fat tissues ($\approx 1.60$ and 50 cm$^{-1}$, respectively), with the water content of ~10%[10,17,32,33]. Tissues of the brain have an exceptionally high content of water. Along with the tissue water, other classes of biomolecules (such as lipids and proteins) play a significant role in formation of the tissue dielectric response at THz frequencies. The assessment of all these biochemical compounds makes it possible to differentiate between normal and pathological tissues of the brain, as well as between different stages of a pathological process relying on the THz spectra and images. All these factors, along with the biochemical and structural neuronal and glial features, including microscopic variations of tissue properties (tissue microenvironments[34], cellular and tissue morphology[35], biomolecules[36] and their large-scale fluctuations[25,37]), make the brain an exciting subject for study using THz technology[10,38,39].

In Fig. 1, dimensions of the structural components in neural tissues (such as neurofibrils, neurons, glial cells, etc.), meninges (pia matter, arachnoid matter and dura matter) and blood vessels are shown at the scale posed by the THz wavelengths. Since traditional THz imaging and spectroscopy systems are based on diffraction-limited optics and obey the $0.5\lambda$ Abbe diffraction limit, the Rayleigh scattering approximation and the effective medium theory are usually applied to describe the THz-wave – neural tissues interactions. Such THz systems allow to study the effective dielectric response of tissues,

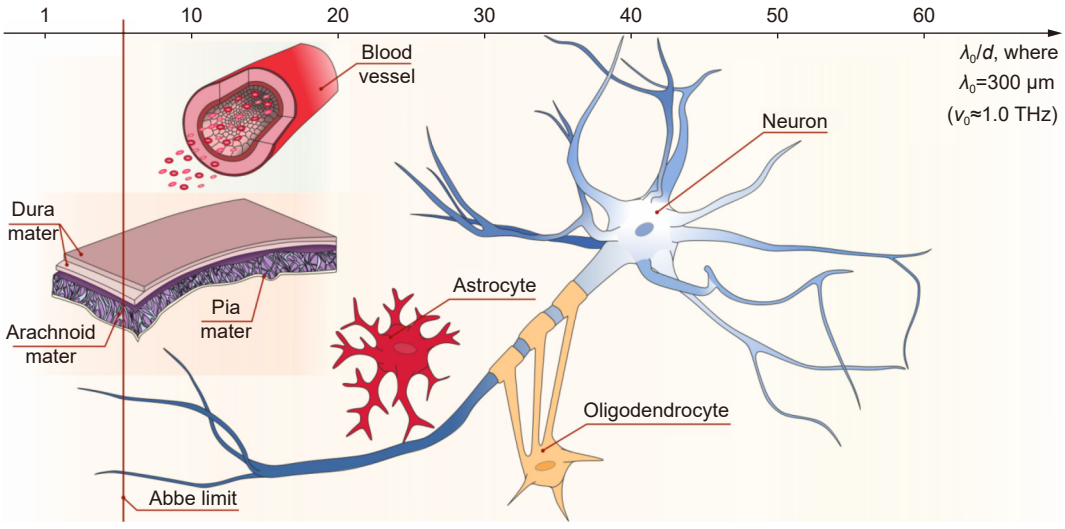


**Fig. 1 | Structural features of brain tissues (neurofibrils, neurons, glial cells, etc.) as well as meninges and blood vessels at the THz-wavelength scale.** The horizontal axis depicts the ratio between the typical size of the structural elements $d$ and the typical free-space wavelength $\lambda_0$= 300 μm ($\nu_0$≈ 1.0 THz), while the vertical solid red line shows the $\lambda$/2-Abbe diffraction limit. Courtesy of G.R. Musina.

which is spatially-averaged over the $\lambda^2$ beam spot area of an optical system[17]. However, dimensions of some structural features of neural tissues are comparable to the THz wavelengths, and modern high-resolution THz optical systems are capable of distinguishing them[40,41]. Studying the effects of Mie scattering on such structural elements of neural tissues and development of novel approaches to describe the THz radiation transport in heterogeneous tissues containing such elements are topical problems of THz biophotonics, which still remain unaddressed[10]. In the general landscape, most of the structural and molecular features of healthy and pathological neural tissues do not affect considerably their electrodynamic response at THz frequencies and, thus, are usually neglected during the THz measurements of tissues[10,17]. Hence, THz complex dielectric permittivities of water, biological liquids and tissues are commonly described by the Debye, Cole–Cole, Davidson-Cole, Havriliak–Negami, or other analytical models of relaxation-like complex dielectric permittivity[21,42–46]. Particularly, the double-Debye model found a wide variety of application in THz biophotonics[10,17,21,46].

In this paper, we start with a brief review of THz optoelectronic systems and measurement principles that are widely applied in biophotonics. Then, we discuss applications of these systems in different branches of neurodiagnostic, such as the diagnosis of neurodegenerative diseases, myelin deficit, tumors and traumatic injuries of the brain. Finally, challenging problems of THz neurodiagnosis are summarized and discussed.

## Methods of tissue spectroscopy and imaging in the THz range

THz spectroscopy and imaging are considered as prospective medical tools due to non-ionizing nature of THz waves and their harmlessness to human body[31], as well as endogenous character of contrast observed between healthy and pathological tissues in THz images and spectra[10,17]. Nowadays, a number of approaches for receiving THz images or spectra of biological tissues are widely applied, that are based on different principles of THz-wave generation and detection[1], rely on either continuous-wave (CW / narrow-linewidth) or pulsed (broadband) radiation, and implement either transmission or reflection measurement geometries.

On the one hand, only thin (100 μm) specimens of hydrated tissues *ex vivo* can be studied in the transmission mode due to a very high THz-wave absorption by tissue water. On the other hand, measurements in the reflection mode require complex calibration procedures in order to reduce the effect of sample displacements during the THz data acquisition, which is especially important when studying tissues *in vivo*[47]. Finally, we notice that, due to the limited depth of THz wave penetration in biological tissues, in neurodiagnosis, only the intraoperative applications of THz technology are possible, when an open access to brain tissues *in vivo* is provided or the freshly-excised brain tissue specimens *ex vivo* are studied. Let us consider several THz experimental spectroscopic and imaging systems that were already applied to study tissues of the brain.

### THz spectroscopy systems

THz spectroscopy is a powerful tool of biophotonics[48–52], that allows analyzing molecular parameters of an analyte and (to some extent) its structural features. Subsequent acquisition and processing of the THz spectroscopic data make it possible to quantify the content and state of many biochemical components of biological tissues (such as water in cells and intercellular matrix), the organization of these components in the morphological plane, as well as kinetics of chemical reactions and physical processes in an analyte[53,54].

The reason for such a widespread use of TPS systems in biophotonics is complete information collected by such systems from a single rapid measurement about the frequency-dependent amplitude and phase of a THz pulse in a wide spectral range[55]. Thus, TPS allows reconstruction of the broadband complex dielectric response (or complex refractive index) of an analyte directly from the measured data, without any additional physical assumptions or the use of the Kramers-Kronig transform[56]. In addition, THz spectroscopy makes it possible to analyze the physical response of an analyte either in the time domain (pulse response function) or the frequency domain (complex transmission or reflection coefficients and complex dielectric permittivity or refractive index)[57]. In Fig. 2, we show examples of TPS systems operating in (a) transmission mode[58–63], (b) reflection mode[64–68], and (c) attenuated total reflection (ATR) configuration[69,70]; all of them are used to characterize biological objects. Transmission mode measurements are usually applied to study thin layers of biological liquids and tissues *ex vivo* sandwiched between the two THz windows[58–63], including their measurements at cryogenic temperatures[59] aimed at unmasking some (other than water) molecular

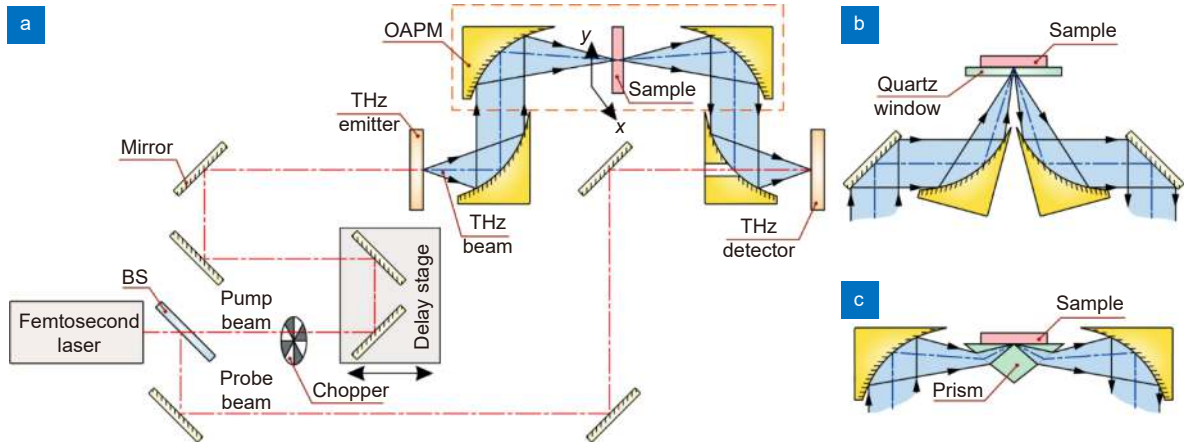


**Fig. 2 | Scheme of the THz pulsed spectrometer.** (**a**) Transmission-mode measurements. (**b**) Reflection-mode measurements. (**c**) ATR configuration. A pair of photoconductive antennas (that rely on photoconductivity/photoswitching effect), nonlinear optical crystals (that rely on optical rectification and electrooptical effects, respectively), or other principles can be used as an emitter and a detector of THz pulses. Here, BS is a beam splitter; OAPM is an off-axis parabolic mirror. Courtesy of G.R. Musina.

properties of tissues. Reflection mode measurements are used to study freshly-excised (hydrated) tissues *ex vivo* and tissue *in vivo*[64–68], where bulk (thick) tissue specimens are considered. ATR geometry is applied to study both bulk tissue specimens and thin layers, down to monolayer of cells. ATR spectroscopy provides high sensitivity, but requires specific calibration procedures. During the TPS measurement, the THz beam path is usually purged by nitrogen gas[63] or even vacuumized[71] to suppress distortion of the THz measurements data by water vapor absorption lines.

Besides TPS, other THz spectroscopy modalities are vigorously explored nowadays and widely applied in different branches of science and technology, as well as have a potential in biophotonics and neurodiagnosis. Among them, we particularly notice

– the Fourier transform IR spectroscopy, that spans the IR and THz ranges and is used mainly in gas spectroscopy, condensed matter physics, and materials sciences[72,73];

– the backward-wave oscillator spectroscopy, that uses CW radiation, spans the GHz–THz range ($< 1.5$ THz), has a narrow linewidth ($10^{-5}\nu$), and is applied in condensed matter physics and physics of magnetism[74];

– the CW THz spectroscopy based on photomixers[75];

– the pulsed THz spectroscopy based on parametric generation and detection in MgO:$LiNbO_3$[76];

– the modern THz pulsed systems with high THz fields to study non-linear optical phenomena[77] and the optical pump – THz probe systems to study photoconductive materials[78].

Meanwhile, all these spectroscopic techniques mostly remain laboratory research tools and are rarely applied to study the THz electrodynamic response of biological tissues and liquids in biophysical laboratories or medical institutions.

## THz imaging systems

Nowadays, THz imaging attracts increasing attention and offers novel opportunities in biomedicine[48–52,79]. Due to the lack of efficient THz detector arrays, majority of THz imaging systems use a single-pixel detector and, thus, involves point-by-point scanning of the sample surface with a focused THz beam of either pulsed or CW radiation followed by processing of thus collected 2D or 3D imaging data.

A widespread use of TPS systems leads to the development of different TPI methods[80]. By studying the time- or frequency-domain response of an object, TPI yields 3D imaging data, that can be represented in form of the spatial distributions of the pulse response function $R(t,\boldsymbol{r})$, broadband complex dielectric permittivity $\tilde{\varepsilon}(\nu,\boldsymbol{r})$, complex refractive index $\tilde{n}(\nu,\boldsymbol{r})$, and others, where $\boldsymbol{r}$ is a radius vector at the imaging plane. Such a comprehensive data about an imaged object open novel opportunities in analysis of the THz electrodynamic characteristics of tissues for subsequent differentiation between normal and pathologically-altered tissues. Various approaches for processing the TPI data were developed, aimed at dimensionality reduction and tissue identification and, thus, meeting the demands of different branches of medical diagnosis[10,17]. Despite such a rich information content, TPI possesses a limited operation rate due to the need of the time-domain TPS waveform

collection at each point of the imaged object. This restrains capabilities of TPI systems in real-time biomedical applications[2].

The key advantage of CW THz imaging systems is a much higher operation rate than that of TPI, but such systems also suffer from lower information content[47]. CW THz imaging can be based on a wide variety of quite-broadband or narrow-linewidth CW THz emitters and detectors and, thus, operating at different frequencies. For example, in refs.[81,82], transmission-mode CW THz imaging system based on 3.4 and 3.7 THz quantum cascade lasers was developed, while in refs.[83,84], a 2.52 THz gas laser was used as a key element during the transmission-mode CW THz imaging (Fig. 3). It is worth noting that reflection-mode and ATR-mode measurement geometries were combined with CW THz imaging principles. Particularly, in refs.[58,85–87], reflection-mode CW THz imaging system based on a 2.52 THz gas laser was developed for biomedical purposes (Fig. 2(b)), while in refs.[88,89], the ATR configuration was implemented for high-sensitive THz measurements of tissues (Fig. 2(c)). The common path CW THz reflection and ATR dual mode imaging system was developed[90]. This dual-mode imaging of common optical path is realized by quickly switching between reflection window and total reflection prism. Finally, in ref.[91], a hybrid CW THz imaging system was developed, that combines active mode (i.e., an object is illuminated by the THz radiation of an external source) and passive mode (i.e., self-emitted THz heat radiation of an object is detected) in order to retrieve maximum information about an object and is aimed at security applications.

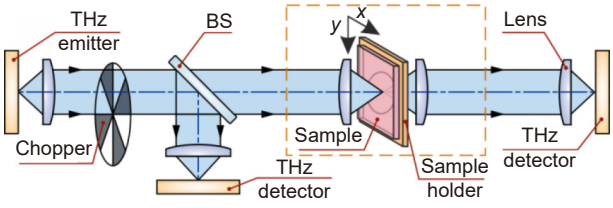


**Fig. 3 | Scheme of representative THz imaging systems operating in transmission mode.** Courtesy of G.R. Musina.

## Superresolution THz microscopy

Modern THz spectroscopy and imaging systems suffer from low spatial resolution, since they usually rely on the lens- or mirror-based optics, the resolution of which obeys the $\simeq 0.5\lambda$ Abbe diffraction barrier of free-space focusing[2,10,17]. Due to large THz wavelengths, resolution of such THz systems is a few hundreds of micrometers or few millimeters, even when working with a very wide-aperture lenses[92,93]. Overcoming the Abbe limit is of particular importance in THz biophotonics and, particularly, neurodiagnosis[10,17,31]. In such applications of THz technology, the limited resolution does not allow to study subwavelength features of neural tissues, detect small-scale neoplasms, accurately delineate the tumor margins, and even locally expose tissues to THz waves.

In order to overcome the Abbe limit, several modalities of superresolution THz spectroscopy and imaging were proposed during the past two decades[94]. Modern methods of THz image reconstruction rely on modeling of the point spread function of an imaging system, followed by the image reconstruction via the deconvolution or inverse filtering[95], or even based on the convolutional neural network approach[96]. All these techniques help to boost the performance of almost any THz imaging system, with the resultant enhancement of resolution by tens of percent, but do not allow to overcome Abbe barrier. Here, we also notice the THz digital holography, synthetic aperture imaging, and computational imaging, which are capable of slightly sub-wavelength resolution, but still cannot overcome the Abbe barrier[97–101]. All these methods have a potential in THz biophotonics, but require complicated techniques to resolve the inverse problems and are accompanied by specific image noises/distortions, which somewhat limits their practical utility.

Next, we consider different modalities of THz scanning-probe near-field optical microscopy (THz-SNOM), which can be classified into the tip- and aperture-based[94]. The tip-based THz-SNOM systems detect the THz field, which is scattered by a metal or dielectric cantilever/tip handled in close proximity to an object, and provides the resolution as high as $10^{-2}$–$10^{-4}\lambda$ thanks to the strong confinement of the THz field on the tip end[102–105]. Several emerging modalities of THz imaging, including wire media[106,107] and high-refractive-index optical fiber bundles[7], can also be assigned to the tip-based THz-SNOM and has a potential for multipixel endoscopic imaging with the resolution down to $10^{-1}\lambda$. In turn, the aperture-based THz-SNOM uses subwavelength diaphragms to either illuminate an object or collect the scattered THz field at its shadow side, with the resultant resolution as high as $\sim 10^{-1}$–$10^{-2}\lambda$ determined by the size of the sub-wavelength aperture[108–110]. As a subtype of the aperture-based THz-SNOM, it is possible to

distinguish the innovative coded-aperture near-field THz microscopy[111] and the laser scanning-point THz source microscopy[112], both of which hold strong potential in THz biophotonics. Despite the superior resolution, all THz-SNOM systems suffer from low energy efficiency due to the use of subwavelength probes in an optical scheme. In this way, to achieve appropriate imaging quality, THz-SNOM systems require powerful emitters, sensitive detectors, and long image acquisition duration. Another disadvantage of THz-SNOM systems is a very small working distance between the probe and an object, due to which the probe may interact with an object, perturb its structure and distort the THz image, or even be damaged itself. Majority of the THz-SNOM systems have limited capabilities in imaging of amorphous media and soft biological tissues, which makes such systems laboratory research tools and restrains their applicability in THz biophotonics.

We particularly notice the solid immersion microscopy principles, that were recently translated from the visible–IR to the THz range[94,113] and, then, adapted for the CW THz imaging of amorphous objects and biological tissues with the resolution down to $0.15\lambda$[40,114]. The essence of the solid immersion effect is a reduction in the dimensions of electromagnetic-beam caustic (focal spot), when the beam is focused in free space at a small distance ($\ll \lambda$) behind the high-refractive-index optical element (i.e., the so-called solid immersion lens), with contribution of both ordinary-propagating and evanescence waves of the total internal reflection. The resolution of the THz solid immersion microscopy appears to be object dependent, but remains strongly subwavelengths in a wide range of the sample optical properties[115]. In ref.[41], a method to resolve the inverse ill-posed problem of the THz solid immersion microscopy was developed. It allows to quantify the spatial distribution of the physical properties of an object over its aperture with superior resolution and, thus, to study sub-wavelength heterogeneities of biological tissues[29,116].

Another approach similar to solid immersion effect is based on dielectric microspheres[94,117–121]. In this approach, a dielectric particle is introduced in the far field of the microscope (i.e., it is handled in front of the focal plane and can be placed either on the surface of an imaged object[117] or in close proximity to it[122]) in order to transfer near-field information and to magnify certain regions of the object. Such virtual images formed by each microsphere are collected with conventional objective lens of the microscope. In ref.[122] white light microscope based on microsphere superlenses demonstrated resolution up to $10^{-2}\lambda$. Since this approach is usually used in transmission light it can be a perspective way for improvement of spatial resolution of THz microscopy of histological brain samples. Here we should also mention waveguide metasurface-based superlens, which allows to overcome the Abbe limit[123]. Such superlens is formed by a gradient array of nanoscale slits perforated in a gold slab, and supports transverse-electric waveguide modes under linearly polarized illumination along the long axis of the slits. These waveguide modes can modulate not only optical phase but also evanescent waves which results in focusing of high-spatial-frequency waves, and thus to the quasi-far-field super-resolution focusing of light. Waveguide metasurface-based superlens developed in ref.[123] provide the resolution as high as $0.24\lambda$.

## Neurodiagnostic application of THz systems

Different modalities of THz spectroscopy and imaging have been already applied to study healthy and pathologically-altered brain tissues from laboratory animals and humans. In this section, we consider the process of THz technology translation to different branches of neurodiagnosis.

### Intact brain

According to the literature data, THz technology was first applied to intact (healthy) brain tissue *ex vivo*. In refs.[81,82,124] possibility of studying the anatomical structure of dehydrated brain tissue using CW THz imaging and near-field microscopy was demonstrated. A contrast between the THz response of gray matter and white matter was demonstrated and attributed to the different content of water, lipids, and proteins in these tissues. The listed factors are in descending order of their influence on the THz response of brain tissues. According to the well-known biochemical properties of brain tissues, in hydrated state (freshly-excised tissues *ex vivo* or tissues *in vivo*), gray matter has high water content and, thus, possesses higher THz refractive index $n$ and absorption coefficient $\alpha$ than those of white matter[125]. On the contrary, as follows from the images of dehydrated rat brain at 3.43 THz (Fig. 4(a–d)), dehydrated white matter has higher THz-wave absorption, which is predominantly due to an absence of water and higher content of lipids[81].

Thus, we can conclude that in the native (hydrated)

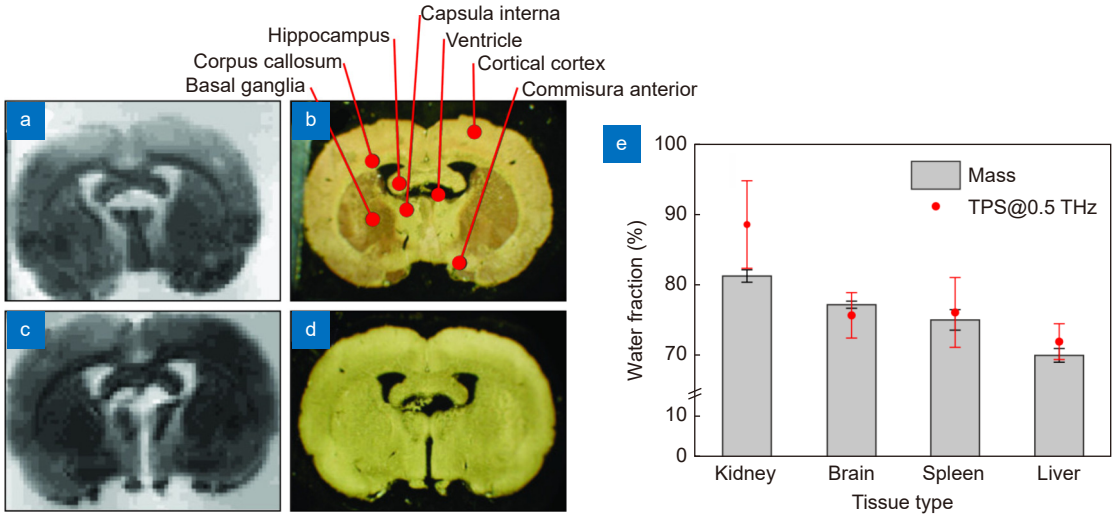


**Fig. 4 | THz measurements data of intact brain *ex vivo*.** (**a–d**) 3.43 THz quantum cascade laser-based images (left column) and visible morphological pictures (right column) of the frontal sections of the dehydrated rat brain *ex vivo*. (**e**) Water content in different freshy-excised (hydrated) tissues from rats *ex vivo* estimated based on the TPS data and tissue weighting (mass). Figure reproduced with permission from: (a) ref.[81], Optical Society of America; (b) ref.[58], under the OSA Open Access Publishing Agreement.

form, the effective THz dielectric response of brain tissue holds information about the content of tissues water. Therefore, THz spectroscopy and imaging can be used to map (qualitatively or quantitatively) this important parameter in healthy and pathological tissues of the brain. As a particular example of the water content estimation, in ref.[58], the authors quantified the fraction of water in freshly-excised intact brain and other tissues from rats using the TPS data at 0.5 THz, while the observed results showed good agreement with those measured by common tissue weighting technique (Fig. 4(e)). In turn, when working with dehydrated (paraffin-embedded or lyophilized) brain tissues, the effective THz optical properties reflect an information about the content of other molecular components of tissues (such as lipids and proteins) and have much lower values of $n$ and $\alpha$.

As shown in Fig. 1, brain tissues are usually assumed to be homogeneous isotropic in THz biophotonics. At the same time, some structural features of the brain and, particularly, of white matter might lead to the structural anisotropy of effective THz optical properties of such tissues. Optical anisotropy of white matter was earlier reported in other spectral ranges[126,127] and attributed to its fiber structure (i.e., the presence of packed bundles of axons with different orientations and degrees of order). The effective optical properties of such systems depend on the mutual orientation of the electromagnetic field polarization and wavevector towards the fibers. In the THz range, the structural anisotropy of white matter can be attributed to the anisotropic dynamic conductivity of electrolyte solution inside the ordered and oriented axons, as well as to the anisotropic character of Mie scattering of THz waves on axons (as mesoscale close-to-cylindrical multilayer dielectric particles). At the same time, the effect of brain tissue optical anisotropy still has not been properly studied in the THz range.

Knowledge about the THz optical anisotropy can be useful in studies of pathological changes in the white matter. The classical method for assessing the local anisotropy of the white matter is a magnetic resonance imaging (MRI)-based diffusion tensor method[127], which considers the anisotropy of water diffusion in tissues and features a limited sensitivity[128]. THz evaluation of the white matter anisotropy can pave the way for more accurate study of the course of conducting fibers in different parts of the central nervous system, which is an important aspect of biomedical research. From the fundamental viewpoint, it is possible to study the connectome of various areas of the brain and the functional aspect (up to the cognitome). To one degree or another, many neurological and neurosurgical diseases have a direct or indirect effect on the properties and state of the white matter. White matter is the primary target of pathogenetic mechanisms in demyelinating diseases and in some forms of traumatic brain injury. At the same time, the white matter can be affected in neurotrauma, acute disorders of cerebral circulation, neurodegenerative, infectious and metabolic diseases[129]. Moreover, tumors grow and infiltrate into various parts of the brain using the white matter tracts as pathways for spreading[130]. Study of

the structural and molecular features of white matter is of great interest for understanding the pathogenetic mechanisms, and THz methods might become the key for solving a number of specific problems in this area.

## Degenerative diseases

There is a demand on a better understanding of degenerative brain disorders. As an example of the neurodegenerative disease, we stress the Alzheimer's disease, which progresses to neurons death in different brain parts because of misfolding and accumulation of protein fractions that form deposits of β-amyloid and disrupting biochemical homeostasis and functional cell spectrum. Alzheimer's disease is a leading cause of dementia, with loss of cognitive functions, memory, thinking skills, which is ultimately resulting in death[131–134]. Cerebrospinal fluid analysis, neuroimaging (e.g., MRI), neuropsychological testing, blood testing, and some other methods have been used for Alzheimer's disease diagnosis. These methods are either time consuming or high in cost[135], and their reliability may depend on the disease severity[136]. Study of the origin, pathways, and contributing factors to neurodegeneration (such as oxidative stress and inflammation[137–139]) is of crucial importance for understanding the progression of neurodegenerative disease and searching of possible therapeutic strategies. Recently, capabilities of THz methods in study of the neurodegenerative diseases were uncovered[59,61,62,68,140–142].

Consider several representative examples of the THz technology applications in study of the Alzheimer's disease. In ref.[59], a difference between the THz absorption coefficient $\alpha$ of frozen intact human brain tissues *ex vivo* and those altered by the Alzheimer's disease was uncovered using the TPS system in conjunction with a closed-cycle cryocooler (Fig. 5(a–c)). It was explained by the different content of β-amyloid, lipofuscin, tau, glial fibrillary acidic protein in pathologically-altered tissues, as well as by the tissue atrophy processes. In ref.[61], it was reported that Tryptophan plays an important role in formation of the THz dielectric response of the Alzheimer-s disease-affected tissues in the *ex vivo* mouse model. In ref.[140], a contrast between the intact animal brain and Alzheimer's disease models became even more clear in the distributions of THz refractive index $n(\boldsymbol{r})$ obtained by TPI (Fig. 5(d–i)). In ref.[62], TPS was combined with the nano-slot patterned metamaterials for highly-accurate probing of the hydration dynamics of β-amyloid aggregates in liquids (Fig. 5(j, k)). For this

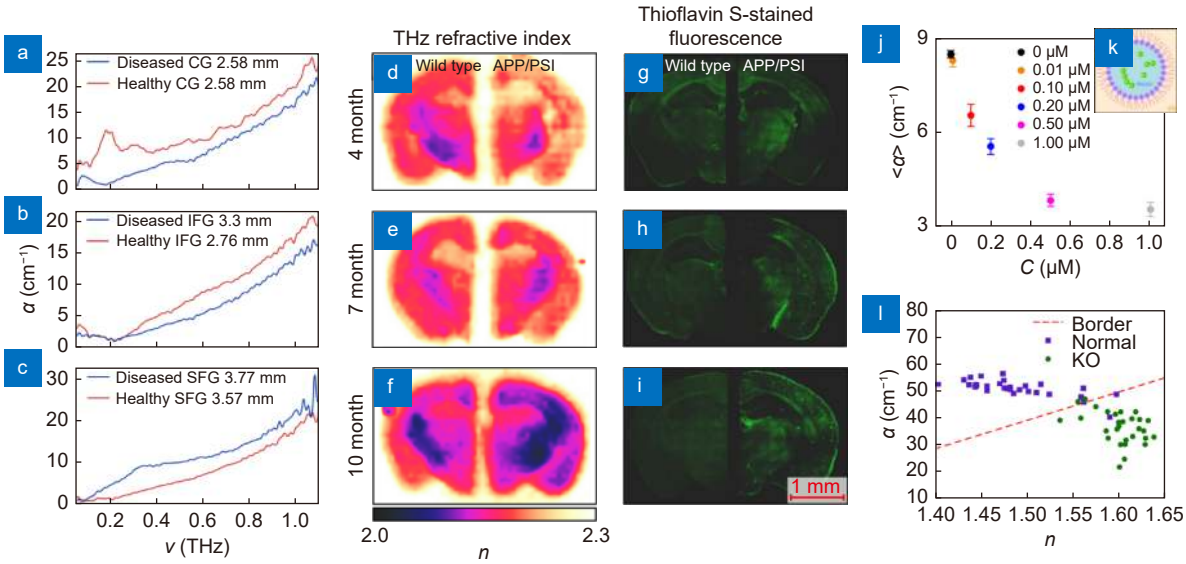


**Fig. 5 | THz measurements data of the Alzheimer's and demyelinating diseases.** (**a**–**c**) THz absorption coefficient $\alpha$ of the intact and Alzheimer's disease-altered tissues of the human brain *ex vivo* obtained at cryogenic temperatures using TPS, where CG, IFG, and SFG stand for the cingulate gyrus, inferior frontal gyrus, and superior frontal gyrus of the brain, respectively. (**d**–**i**) THz refractive index distributions $n(\boldsymbol{r})$ measured by TPI (left) and Thioflavin S-stained fluorescence images (right) of the wild-type and APP/PS1 Alzheimer's disease models depending on age. (**j**, **k**) Averaged THz absorption coefficient $\alpha$ of a liquid buffer with β-amyloid aggregates-containing nanodroplets, as well as the sketch of a single nanodroplet with a β-amyloid aggregate. (**l**) THz refractive index $n$ and absorption coefficient $\alpha$ obtained from the myelin deficit (Rheb1 KO) and normal mice brains *ex vivo*. Figure reproduced with permission from: (a–c) ref.[59], IET; (d–i) ref.[140], (j, k) ref.[62] Elsevier; (l) ref.[68], under a Creative Commons Attribution 4.0 International License.

aim, β-amyloid aggregates-containing water nanodroplets were used for improved THz sensing. The integration of a metamaterial sensor and nanoconfined droplets allowed to enhance the sensitivity of THz measurements (up to 1 nM of β-amyloid aggregates in a buffer solution). The observed results are of high importance because the amyloid β peptide and its ordered aggregates are associated with the onset of the Alzheimer's disease, and, thus, they are considered as biomarkers for diagnostic and therapeutic applications. In ref.[141], the nature of the THz conductivity changes during biochemical evolution of the β-amyloid with different concentrations (from monomers to polymer fibrils) were studied using the near-field THz spectroscopy. It was found that the THz conductivity decreases with the evolving fibrillization states and increases with the elevating molar concentrations. To further identify markers underlying the contrast between intact and pathologically-altered brain tissues in the THz range (without taking into account the effect of water), the authors of ref.[142] measured dehydrated tissue samples. In post-mortem tissues, a considerable difference was found between the THz reflectivity of normal brain fragments and Alzheimer's disease, and the contrast was especially pronounced for white matter. This difference was explained by the concomitant demyelination.

Another degenerative disease to be considered is a demyelinating disease that occurs most often in young patients as the most socially-active group of the population. In ref.[68], TPS was combined with chemometric analysis to study the models of the demyelination process in the paraffin-embedded brain of mice and rhesus monkeys *ex vivo*. From Fig. 5(l), we notice a contrast between the myelin deficit and normal mouse brain *ex vivo* represented in the $n$–$\alpha$ space.

## Tumors

THz technology is considered as a prospective tool of the intraoperative diagnosis of human brain tumors[38], with an emphasis on gliomas, which are among the most common and deadly pathologies of the brain, constituting ≃ 26% of all primary brain tumors and ≃ 81% of malignant primary brain tumors[143]. Gliomas are classified by the World Health Organization (WHO) into the WHO Grades I to IV, where Grades I, II and III, IV stand for the low- and high-grade gliomas, respectively[144]. Glioblastoma (WHO Grade IV glioma) is the most dangerous tumor of the brain, with the five-year relative survival rate of only ≃ 6.8%[143]. Surgery is the mainstay of the glial tumors' treatment, the main goal of which is a gross-total resection of a tumor with maximal preservation of surrounding intact tissues[145]. Gliomas usually have unclear margins, that complicate their gross-total resection. In many cases, accurate delineation of glioma margins can be provided only by the *ex vivo* histopathological examination of the excised tissues, using the hematoxylin and eosin (H&E)-stained histology aided by the molecular sensing and genetics[146]. Such examination of excised brain tissues can be performed either intraoperatively (thus, extending the terms of surgery) or postoperatively (aimed at making a definitive molecular pathological diagnosis). Despite histopathology remains a gold standard in tumor diagnosis, we notice an increasing demand for the novel methods of the rapid intraoperative detection of tumor margins.

Common methods of the pre-operative imaging (MRI, computed tomography, and positron emission tomography) do not provide reliable accuracy of the tumor margins detection due to the brain shifts, caused by the dura mater opening, tumor removal, brain tissue edema, and cerebrospinal fluid losses[147]. Thus, real-time imaging techniques (intraoperative ultrasound and MRI) were developed[148]. However, these instruments suffer from low spatial resolution, while their integration into modern neurosurgical workflows remains labor intensive and expensive. Other intraoperative neuroimaging methods are fluorescent-based techniques involving the use of the 5-aminolevulinic acid-induced fluorescence of protoporphyrin IX[149], fluorescein sodium[150], or other fluorophores. They are inexpensive and provide high sensitivity for high-grade gliomas and meningiomas, but their sensitivity drops for the pediatric and low-grade tumors[151]. Optical coherence tomography[152,153], Raman spectroscopy and imaging[154], confocal and polarization-sensitive microscopy[155], visible and near-IR spectroscopy[156], as well as photoacoustic imaging[157] are vigorously explored, as tools for the intraoperative brain tissue imaging, but still remain far from clinical practice. Efficiency of these methods is restrained by a number of factors, such as the aforementioned application of contrast agents, limited sensitivity and specificity, and high labor intensity.

### Glioma models from mice and rats

A potential of THz technology in the intraoperative diagnosis of brain tumors was studied by the THz

spectroscopy and imaging of different tumor models from rats and mice[38]. In ref.[35], orthotopic glioma model from rats was imaged *ex vivo* using the reflection-mode TPI system. The observed THz images revealed a difference between intact tissues and a tumor in both freshly-excised and paraffin-embedded (dehydrated) states. In Fig. 7(a–i), visible, THz, and MRI images of the freshly-excised orthotopic glioma samples are compared. For the freshly-excised tissues, the difference between intact ones and a tumor was attributed to the increased content of tissue water in a tumor, which is due to the abnormal microvascularization, edema, and body fluids around necrotic debris. For the paraffin-embedded tissues, the contrast is less pronounced and originates reportedly from changes in cell density in a tumor. In ref.[60], TPS was applied to study paraffin-embedded intact tissues and glioma model (GL261 cell line) from mice *ex vivo*. The observed THz dielectric spectra justified a contrast between paraffin-embedded intact tissues and a tumor in the THz range. Next, we stress remarkable results of ref.[67], the authors of which applied TPS to study the freshly-excised and dehydrated intact tissues and glioma model (C6 cell line) from rats *ex vivo*. The measured THz dielectric spectra were analyzed using a linear spectrum decomposition approach, which revealed an increased water content in a tumor and, thus, justified water as the main reason of endogenous contrast between healthy tissues and a tumor. Finally, in refs.[66,85,86], different methods of THz spectroscopy, reflectometry and imaging were applied for discrimination between intact brain tissues and tumors, involving *ex vivo* and *in vivo* glioma models from mice and rats (eGFP+GSC-11, C6, and U87-MG cell lines), as well as few samples of high-grade gliomas from humans.

Recently, different approaches of boosting the THz imaging of brain tissues were proposed. First, in ref.[89], temperature-dependent transmission-mode TPS and 2.52 THz CW ATR imaging were used to study orthotopic glioma model from mice *ex vivo*. In Fig. 6(j–o), representative THz images are shown, that were collected in the temperature range from −20 to 35 °C, compared with a visible photo, and verified by the H&E-stained histology. It was found that THz response varies, as a function of temperature, in a different manner for intact tissues and a tumor. Such a temperature-dependent character of the tissue response at THz frequencies can be used for the improved differentiation between intact tissues and a tumor. Furthermore, some optimal temperatures of a tissue specimen *ex vivo* can be selected to improve a contrast between healthy and pathological brain tissues in the THz range (similar effect was observed earlier for the TPS and TPI measurements of

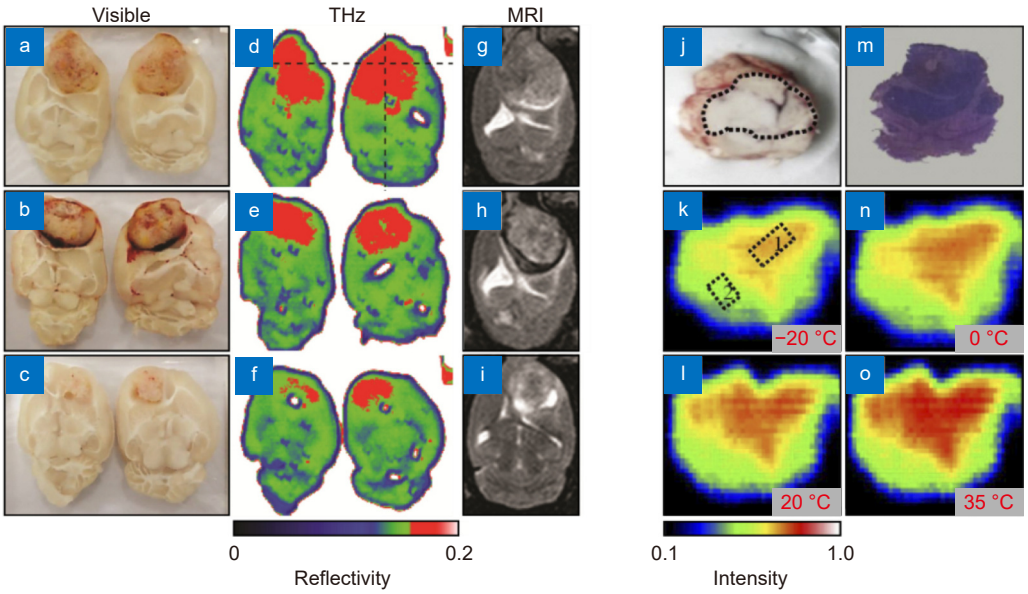


**Fig. 6 | THz imaging of brain glioma models from laboratory animals *ex vivo*.** (**a–i**) Visible, THz, and MRI images of orthotopic glioma model from rats, where the THz image dimensions and resolution are 4 cm×3 cm and 250 μm, respectively. (**j–o**) Visual image, H&E-stained histology and temperature-dependent 2.52 THz CW ATR images of orthotopic glioma model from mice *ex vivo*, where the sample temperature varies in the range from −20 to 35 °C. In (**k–o**), the blue boarder marks the boundary between background and a sample; while in (k), boxes 1 and 2 point areas of healthy and tumorous tissues. Figure reproduced with permission from: (a–i) ref.[35], Optical Society of America; (j–o) ref.[89], under the Optica Open Access Publishing Agreement.

mucosa cancer[26]). Second, to enhance the accuracy of the tumor margins delineation, in ref.[87], a region-of-interest (ROI) segmentation method was developed for work with the 2.52 THz CW imaging system. This method combines a variety of signal processing techniques, including the block matching 3D denoising, fuzzy c-means clustering, morphology operation, and canny edge detection. It was first verified involving test objects with sharp reflectivity changes and then applied to detect margins of rat glioma model *ex vivo* with quite smoothed margins. The observed results highlight a potential of the CW THz imaging and the proposed hybrid ROI segmentation method in brain tumor diagnosis.

**Human brain gliomas**

Glioma models from animals only partially mimic structural and biophysical properties of human brain gliomas. Therefore, in ref.[64], TPS was applied to study the THz dielectric response of gelatin-embedded intact tissues, edematous tissues, and WHO Grades I–IV gliomas of the human brain *ex vivo*. To preserve tissues from hydration/dehydration, retain their original molecular properties during the THz measurements, and, thus, sustain their THz response unaltered (as compared to the freshly-excised tissues), gelatin slabs were used for the tissue fixation[158]. In Fig. 7, the measured THz optical properties are represented in form of the tissue refractive index $n$ and absorption coefficient $\alpha$, where statistical differences between intact tissues and gliomas of all WHO grades are evident. However, the THz response of edematous tissue appears to be very similar to that of a tumor, while there is also no significant contrast between the response of gliomas of the different grades. Thus, the THz response of human brain tissues *ex vivo* from ref.[64] confirmed earlier results of the aforementioned studies, that involved THz measurements of gliomas models from mice and rats (Section *Glioma models from mice and rats*). Furthermore, the data from ref.[64] were qualitatively verified in recent research work, where the TPS ATR measurements and the 2.52 THz CW ATR imaging of intact tissues and WHO Grade I–IV gliomas from humans were performed[69,88]. Indeed, THz methods hold a potential in the intraoperative differentiation between intact tissue and gliomas of the human brain.

High dispersion of the experimental $n$- and $\alpha$-spectra (Fig. 7) was attributed to heterogeneous character of tissues. Particularly, in ref.[64], intact brain tissues were not differentiated into the white matter and gray matter, which might be the reason of higher dispersion for the intact tissues. In turn, the dispersion of glioblastoma optical properties reportedly originates from the presence of tissue heterogeneities due to necrotic debris, which is inherent to this type of tumor. Such tissue heterogeneities might be specific for various human brain tumors,

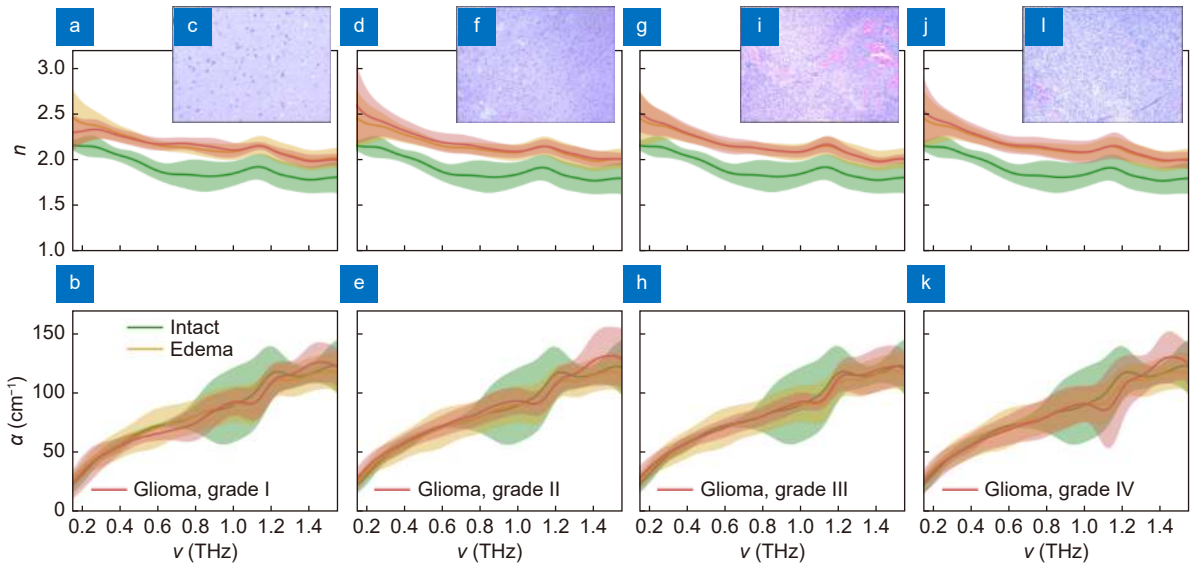


**Fig. 7 | Spectra of the THz refractive index $n$ and absorption coefficient $\alpha$ (by field), as well as H&E-stained histology of intact tissues, edematous tissues, and gelatin-embedded human brain gliomas *ex vivo* of the different WHO Grades.** (**a**–**c**) Grade I. (**d**–**f**) Grade II. (**g**–**i**) Grade III. (**j**–**l**) Grade IV. THz optical properties of gliomas are compared with equal data for intact and edematous tissues, where the error bars represent a ±2.0$\sigma$ confidential interval of measurements ($\sigma$ is a standard deviation). Figure reproduced with permission from ref.[64], under a Creative Commons Attribution 4.0 Unported License.

forming a subject of additional comprehensive research work (it will be addressed below, to some extent). Non-monotonic dispersion at lower (at $< 0.3$ THz) and higher ($> 0.8$ THz) frequencies is due to the measurement errors originating from fluctuations of humidity along the THz beam path, limited resolution of TPS, as well as the drops of the TPS system sensitivity at low and high frequencies.

Next, in ref.[65], THz dielectric response of freshly-excised intact tissues, edematous tissue, and WHO Grades I–IV gliomas of the human brain *ex vivo* was analyzed using relaxation models of complex dielectric permittivity. Particularly, the double-Debye (DD) model, which is based on a pair of the Debye relaxators, and the double-overdamped-oscillator (DO) model, which includes a pair of the Lorentz oscillators with a high damping constant, were considered. The DD model has the form[46]

$$\tilde{\varepsilon} = \varepsilon_\infty + \frac{\Delta\varepsilon_1}{1+\mathrm{i}\omega\tau_1} + \frac{\Delta\varepsilon_2}{1+\mathrm{i}\omega\tau_2}\,, \tag{1}$$

where $\omega = 2\pi\nu$ is an angular frequency, $\Delta\varepsilon_1$, $\Delta\varepsilon_2$ are magnitudes that regulate a contribution of the "slow" and "fast" Debye relaxations with their time constants $\tau_1$, $\tau_2$, respectively, $\varepsilon_\infty$ is a high-frequency constant dielectric permittivity at $\nu \gg (2\pi\tau_{1,2})^{-1}$. The DD model is common for THz biophotonics. It allows accurate parameterization of the THz spectroscopic data for water, water solutions, biological liquids, and tissues[10,17], for which only 5 independent parameters are required – namely, $\varepsilon_\infty$, $\Delta\varepsilon_1$, $\Delta\varepsilon_2$, $\tau_1$, and $\tau_2$.

In turn, the DO model is novel for THz biophotonics. It has the form[159]

$$\tilde{\varepsilon} = \varepsilon_\infty + \frac{\Delta\varepsilon_1}{1-\dfrac{\omega^2}{\omega_{01}^2}+\mathrm{i}\dfrac{\omega\gamma_1}{\omega_{01}^2}} + \frac{\Delta\varepsilon_2}{1-\dfrac{\omega^2}{\omega_{02}^2}+\mathrm{i}\dfrac{\omega\gamma_2}{\omega_{02}^2}}\,, \tag{2}$$

where $\Delta\varepsilon_1$, $\Delta\varepsilon_2$, $\omega_{01}$, $\omega_{02}$, and $\gamma_1$, $\gamma_2$ stand for magnitudes, quasi-resonant frequencies (given by the restoring forces) and damping constants, respectively, of the "slow" and "fast" relaxations, which are equivalent to the "slow" and "fast" Debye relaxations (Eq. (1)). A constant $\varepsilon_\infty$ and a magnitude $\Delta\varepsilon_j$ of $j$-th Debye relaxation are equal to those of a corresponding overdamped oscillator. One can also calculate other parameters of $j$-th overdamped oscillator based on corresponding Debye relaxator:

$$\gamma_j = \omega_{0,j}^2\tau_j,\ \gamma_j = C\omega_{0,j},\ C \gg 1\,, \tag{3}$$

here, $C$ is a constant, the particular value of which is not so important, unless it is much larger than unity. In ref.[65], this constant was $C = 10^2$. The DD and DO models provide almost equal values of complex dielectric permittivity $\tilde{\varepsilon} = \varepsilon' - \mathrm{i}\varepsilon''$ (or complex refractive index $\tilde{n} = n - \mathrm{i}c_0\alpha/(2\pi\nu)$, where $c_0 \approx 3\times10^8$ m/s is the speed of light in free space, and $\alpha$ is the absorption coefficient, by field) at low-frequencies up to $\omega \sim (2\pi\tau_i)^{-1} < \omega_{0,i} \ll \gamma_i$. At the same time, at higher frequencies $\omega > (2\pi\tau_i)^{-1}$, the DD model gives non-physical high loss, due to which this model does not satisfy the sum rule and predict infinite number of charged carriers underlying the dielectric response of matter. In turn, the DO model satisfies the sum rule and, thus, seems to be more physically rigorous[65].

Based on the THz dielectric spectra from Fig. 7 and ref.[64], parameters of the DD and DO models were calculated in ref.[65]. They are shown in Tab. 1, where, for all the considered tissues, the "slow" and "fast" relaxation times $\tau_1$, $\tau_2$ were set equal to those of free water from ref.[46]. The observed higher magnitudes of the "slow" and "fast" relaxations $\Delta\varepsilon_1$, $\Delta\varepsilon_2$ for all glioma grades (Table 1) are attributed to the higher content of polar $H_2O$ molecules in a tumor than that in intact tissues[160]. The developed DD and DO models can be used to describe the THz-wave – brain tissue interactions in different branches of THz biophotonics using analytical or numerical methods of electrodynamics. Moreover, parameters $\varepsilon_\infty$, $\Delta\varepsilon_1$ and $\Delta\varepsilon_2$ of these models can serve as physically-reasonable principal components for the differentiation between normal and pathologically-altered brain tissues, as detailed in ref.[161].

Next, water content in intact tissues and WHO Grade I–IV gliomas of the human brain *ex vivo* was estimated relying on the sum rule[65]

$$f = \frac{N_{\text{tissue}}}{N_{\text{water}}} = \frac{\int_{\omega_{\min}}^{\omega_{\max}} \omega\varepsilon''_{\text{tissue}}\mathrm{d}\omega}{\int_{\omega_{\min}}^{\omega_{\max}} \omega\varepsilon''_{\text{water}}\mathrm{d}\omega}\,, \tag{4}$$

where integration of imaginary part $\varepsilon''$ of the complex dielectric permittivity within the considered spectral range $(\omega_{\min}, \omega_{\max})$ is involved for tissues, in the numerator, and for a liquid water, in the denominator. The obtained water content estimates are shown in Fig. 8, from which we notice that the water content is 71.1±6.8% for the intact tissues, while that in edema and WHO Grade I–IV gliomas is ~ 510% higher. From Fig. 8, we also notice that the obtained values of water content overall agree with the data from ref.[162–165], that were measured using TPS or other experimental techniques.

**Table 1 | The DD model parameters for water, intact tissues, edematous tissues, and WHO grades I–IV gliomas. The DO model can be calculated based on these parameters using Eqs. (2) and (3). Reproduced from ref.[65] with the permission of Optica Publishing.**

| | $\varepsilon_\infty$ | $\tau_1$(ps) | $\Delta\varepsilon_1$ | $\tau_2$(ps) | $\Delta\varepsilon_2$ |
|---|---|---|---|---|---|
| Water from ref.[46] | 4.10 | | 72.20 | | 2.50 |
| Intact tissue | 2.29±0.29 | | 49.82±2.17 | | 1.80±0.33 |
| Edema | 3.48±0.29 | | 61.37±9.39 | | 1.58±0.40 |
| Grade I | 3.29±0.38 | 10.60 | 50.54±11.55 | 0.18 | 1.93±0.50 |
| Grade II | 3.40±0.24 | | 61.37±12.27 | | 1.93±0.38 |
| Grade III | 3.32±0.11 | | 56.32±7.22 | | 2.03±0.33 |
| Grade IV | 3.30±0.22 | | 58.48±9.38 | | 2.00±0.28 |

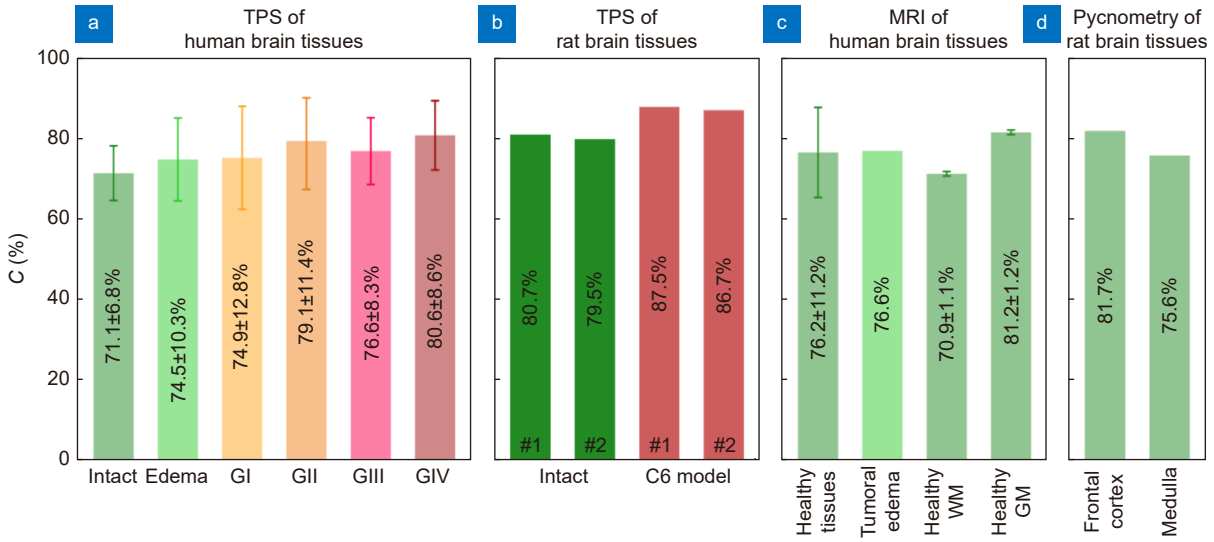


**Fig. 8 | Water content in healthy and pathological tissues of the brain measured using different experimental techniques.** (**a**) Intact tissues, edema, and WHO Grade I–IV gliomas (GI–GIV) of the human brain *ex vivo* measured by TPS in ref.[65]. (**b**) Intact tissues and C6 glioma model from rat brain *ex vivo* measured by TPS in ref.[67]. (**c**) Healthy human brain tissues and tumoral edema *in vivo* measured by MRI in refs.[162–164], where WM and GM stand for white matter and gray matter, respectively. (**d**) Healthy rat brain tissues *ex vivo* measured by pycnometry in ref.[165]. Here, error bars represent fluctuations of water content within the considered set of tissue specimens. Figure reproduced with permission from ref.[65], under the OSA Open Access Publishing Agreement.

## Molecular markers of gliomas

Despite water remains the main endogenous marker of neoplasms in the THz range[10], establishing a relationship between the tissue response at THz frequencies and the well-known molecular markers of a tumor (other than water) is a challenging problem of THz biophotonics, since the role of such markers in modern oncology increases dramatically and even become decisive. Consider several important pathogenetic and clinical molecular events that are increasingly used in brain tumor diagnosis along with the common classification of gliomas into the abovementioned WHO Grades I–IV:

**Ki-67 labeling index.** Proliferation is the most important function of cells of any neoplasm, which determines the malignant potential of a tumor. In the pathological diagnosis of tumors, the Ki-67 marker is used to assess this function[166,167]. This protein is involved in direct preparation for cell division and, with a high degree of accuracy, marks cells preparing to enter the process of mitosis. This marker has confirmed its high predictive value, independent of other histological criteria, for a number of tumors, including diffuse gliomas[168,169]. The assessment of the Ki-67 labeling index level plays a decisive role in formulation of the pathohistological diagnosis and determining the tactics of further treatment[168,169]. The activation of the cells' proliferative program affects inevitably their metabolic profile. One of its biochemical consequences is a change in the amount and state of tissue water, which is especially noticeable under conditions of accelerated pathological cell division in the framework of carcinogenesis processes[170].

**Mutations in the isocitrate dehydrogenase genes (*IDH1* and *IDH2*).** For diffuse glial tumors, the mutational status of the *IDH1* and *IDH2* genes became the de-

fining diagnostic parameter[171,172]. These mutations act as the earliest molecular events in diffuse gliomas and determine the further course of carcinogenesis. The presence of these mutations has an extremely pronounced positive effect on the prognosis of patients with diffuse gliomas[171,172]. The influence of *IDH1* and *IDH2* mutations on the processes of nucleation and development of tumors is mediated by metabolic factors. An indirect feature of these modifications is the change in the state and content of water in tumor cells.

**Methylation of the O⁶-methylguanine–DNA methyltransferase (*MGMT*) gene promoter.** A molecular parameter of high diagnostic value is the methylation status of the promoter region of the *MGMT* gene. This molecular event refers to epigenetic modifications that regulate genome expression. Methylation of the *MGMT* gene promoter is associated with profound changes in the molecular and functional status of tumor cells. It serves as an independent favorable prognostic factor for survival of patients with diffuse gliomas[173,174]. Methylation of the *MGMT* gene promoter is accompanied by deep metabolic rearrangements in tumor cells associated with a change in the protein composition of tumor cells, which entails modifications in the content and state of intracellular water due to the polarity of most protein molecules.

There are some prerequisites to study the listed molecular markers of gliomas using the THz methods and other modern optical modalities of tissue spectroscopy and imaging, for which either freshly-excised or fixed tissues *ex vivo* can be considered. In ref.[69], it was demonstrated that the *IDH* mutant and wild-type glioma tissues can be distinguished by TPS arranged in the high-sensitive ATR configuration. From Fig. 9, we notice that THz spectroscopy has a potential for a rapid molecular typing of glioma tissues for this important diagnostic factor. In ref.[175], THz absorption spectra $\alpha$ of 2-Hydroxyglutaric acid disodium salt (2HG) are investigated. 2HG is another biomarker existing in glioma, which can serve for differentiation between tumor and normal tissue. Authors revealed correlation between THz absorption spectra and molecular structure of the 2HG isomers.

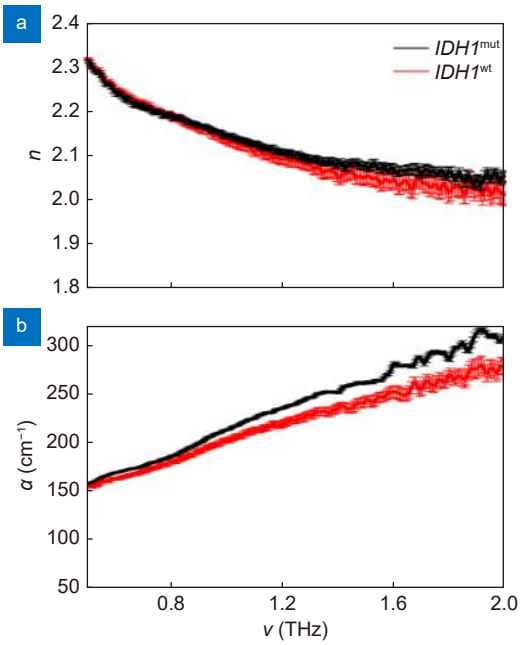


**Fig. 9 | THz optical properties of *IDH1* wild-type sample and *IDH1* mutant positive sample.** (**a**) Refractive index *n*. (**b**) Absorption coefficient $\alpha$. Figure reproduced with permission from ref.[69], under the Optica Open Access Publishing Agreement.

## Brain tissue heterogeneity

In order to study heterogeneities of healthy and pathological brain tissues at the THz-wavelength scale, in refs.[41,116], TPS measurements and quantitative superresolution 0.6 THz CW solid immersion microscopy (with the spatial resolution as high as $0.15\lambda$)[94] of freshly-excised intact tissues and glioma model 101.8 from rats *ex vivo* were performed. The homograft glioma model 101.8[176] involves injection of rat brain glioma tissues into the brain of another rat. This model was obtained and is kept in the collection of the Research Institute of Human Morphology (Moscow, Russia). It is compliant with glioblastoma (WHO Grade IV glioma)[144] and widely applied in experimental neurooncology. Glioma 101.8 is heterogeneous in nature and mimics unclear (diffuse) margins and tissue heterogeneities (such as areas of necrosis, hemorrhages, and microvascularity), that are usual to the human brain gliomas. Therefore, glioma 101.8 is a perfect candidate for evaluating the performance of novel modalities of brain tissue spectroscopy and imaging[152,153].

In Fig. 11(a–c), THz refractive index *n* and absorption coefficient $\alpha$ (by field) are shown for the freshly-excised intact rat brain and glioma *ex vivo*, measured by a diffraction-limited TPS system and verified by the H&E-stained histology[116]. Mean THz optical properties and their spatial dispersion over the rat brain are shown by markers and error bars, respectively. Due to the limited TPS resolution, intact tissues were not differentiated into the white matter and grey matter, and no subwavelength neurovascular structures and heterogeneities of the brain were identified. TPS data from Fig. 11(a, b) confirmed

endogenous contrast between intact tissues and glioma 101.8 from rats *ex vivo* in the THz range, which is similar (but less pronounced) to that observed earlier for distinct xenograft glioma models from laboratory animals (Section *Glioma models from mice and rats*)[60,66,67,85,86] and humans (Section *Human brain gliomas*)[64,65,69,88]. Also, from Fig. 11(a, b), considerable dispersion of the measured THz optical properties across the sample is notable for both the intact tissues and a tumor[116], which is similar to observations of glioma model (Fig. 7(a–i))[35] and human brain gliomas (Fig. 7)[64]. As mentioned above, such heterogeneity is assumed to originate from various neurovascular structures, fluctuations of the water content and cell density over the brain, but the diffraction-limited resolution of common TPS systems fails to justify the nature of such tissue features.

This problem was addressed using the quantitative superresolution 0.6 THz ($\lambda \approx 500$ μm) microscopy in refs.[41,116]. Figure 10(d–o) show results of studying intact tissues and glioma 101.8 in form of the visible photo, THz intensity image $I(\boldsymbol{r})$, refractive index distribution $n(\boldsymbol{r})$, absorption coefficient distribution $\alpha(\boldsymbol{r})$, water content distribution $C(\boldsymbol{r})$, and H&E-stained histology, as detailed in ref.[41]. The observed subwavelength distributions of the THz optical properties $n(\boldsymbol{r})$, $\alpha(\boldsymbol{r})$ and tissue water content $C(\boldsymbol{r})$ agree with the average values measured by the diffraction-limited TPS systems (Figs. 8 and 11(a, b))[64,65,67,116]. Meanwhile, thanks to the superior resolution of the THz microscope, considerable heterogeneity of the brain tissues is evident.

From THz images in Fig. 10(d–o), a pronounced difference is observed between the white matter and gray matter, which is consistent with previous observations[35,68]. Particularly, white matter possesses higher THz refractive index $n$ and absorption coefficients $\alpha$ due to an increased content of both tissue water $C$ (in the form of an electrolyte solution inside axons) and myelin (a lipid-rich substance that surrounds the axons). Tumor also

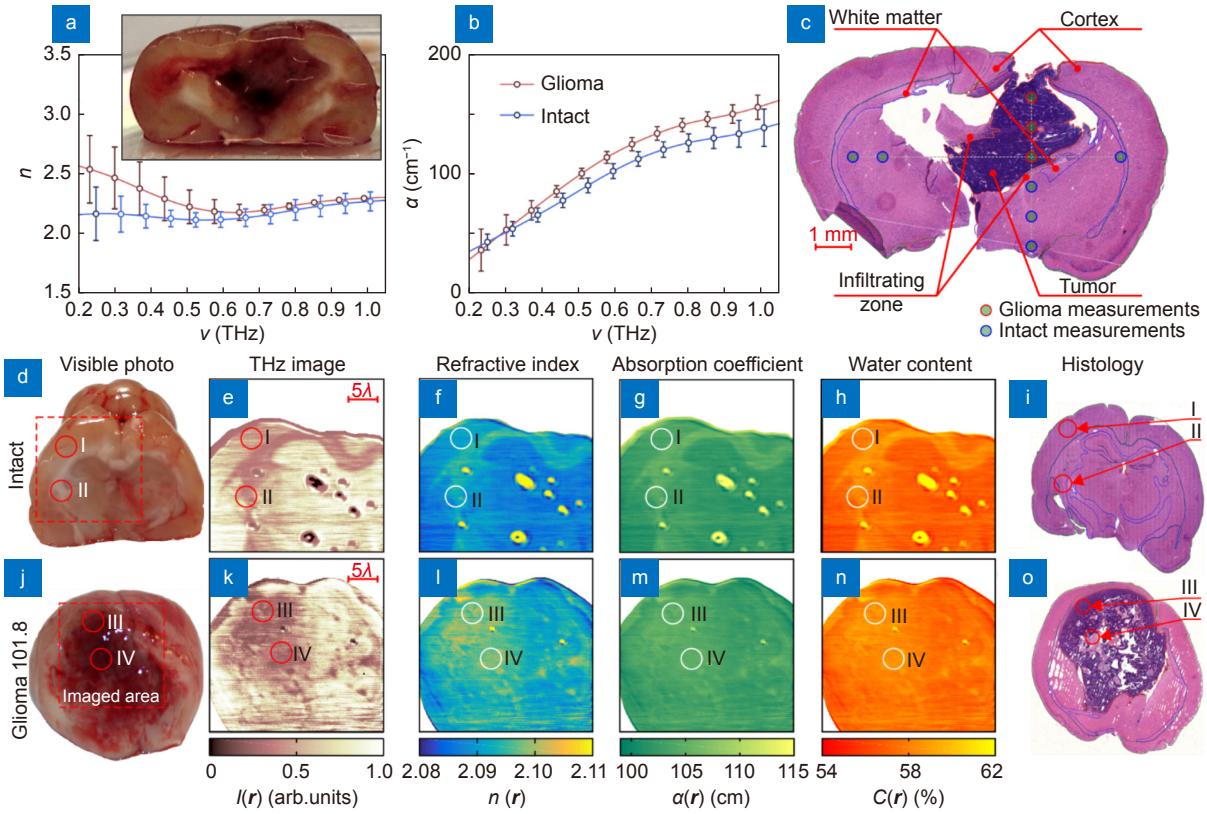


**Fig. 10 |** The data of TPS measurements and quantitative superresolution CW THz solid immersion microscopy (at $\nu = 0.6$ THz or $\lambda \approx 500$ μm) of the freshly-excised intact brain and glioma model 101.8 from rats *ex vivo*. (**a–c**) Effective THz refractive index $n$ and absorption coefficient $\alpha$ (by field) of intact tissues and a tumor, measured by TPS and verified by H&E-stained histology. (**d–i**) Visible photo, THz image $I(\boldsymbol{r})$, refractive index distribution $n(\boldsymbol{r})$, absorption coefficient (by power) distribution $\alpha(\boldsymbol{r})$, water content distribution $C(\boldsymbol{r})$, and H&E-stained histology, respectively, for the intact tissues. Here, $\boldsymbol{r}$ is a radius vector at the imaging plane; markers I, II point the gray matter (cortex) and white matter, respectively. (**j–o**) Equal data set for a tumor, where markers III, IV indicate the tumor cells accumulation and the necroses zone. Figure reproduced with permission from: (a–c) ref.[116], (d–o) ref.[41], under the OSA Open Access Publishing Agreement.

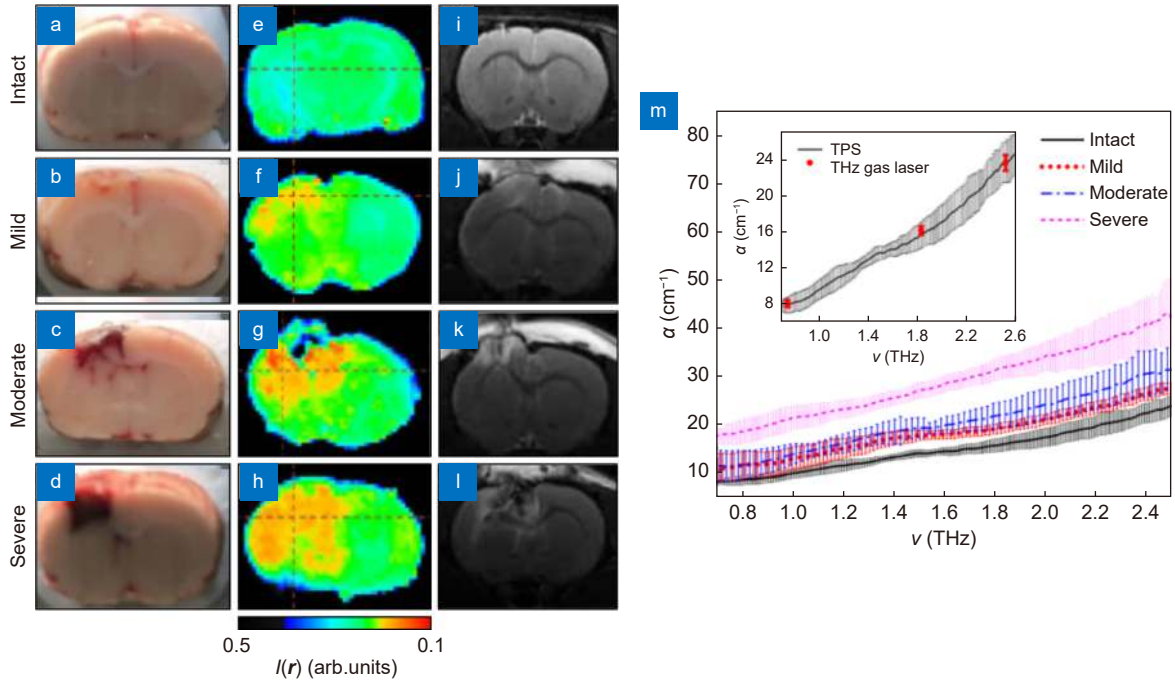


**Fig. 11 | Results of the THz measurements *ex vivo* of the freshly-excised intact rat brain and those with TBI models of the different degrees.** (**a–l**) Visible, THz, and MRI images of freshly-excised intact rat brain and TBI models of the mild, moderate, and severe degrees. (**m**) Spectra of the absorption coefficient $\alpha$ of the paraffin-embedded brain samples from intact rat brain and TBIs. Figure reproduced with permission from ref.[83], SPIE.

possesses higher $n$- and $\alpha$-values than those of intact tissues owing to higher water content $C$ in a tumor[65,67]. A considerable mesoscale heterogeneity of a tumor is also notable, originating from the tumor cells' accumulations, vessels, necrotic debris, and hemorrhages[41,116].

On the one hand, the observed results of the THz microscopy of the rat brain *ex vivo* justify a label-free contrast between intact tissues and a tumor. On the other hand, the THz images highlight considerable heterogeneity of brain tissues at the THz-wavelength scale. This poses important problems of studying the effects of Mie scattering of THz waves in brain tissues and adapting the radiative transfer theory for the needs of THz biophotonics and neurodiagnosis. Indeed, both absorption and scattering effects can considerably impact the THz-wave transport in healthy and pathological tissues of the brain. These scattering effects might either complicate the THz diagnosis of tumors (they can lead to strong variability of the effective THz response of tissues) or become a source of additional useful information for the tissue differentiation. Particularly, such structural features of a tumor, as areas of necrosis and hemorrhages, are typical for glioblastoma and, thus, can be used as a source of additional information for the differentiation between glioblastoma and other benign and malignant gliomas.

### Other applications in neurooncology

Although most research papers focus on THz spectroscopy and imaging of brain gliomas, as the most common and dangerous tumors of the brain, THz technology has a potential in the intraoperative diagnosis of other types of primary and secondary brain tumors. For example, in ref.[177], an ability for the differentiation between intact tissues and human brain meningioma of the WHO Grade I was uncovered using TPS, but this study involved only one sample of a tumor. Attractiveness of THz technology in diagnosis of other types of human brain tumors should be further confirmed, since it requires collections and analysis of the THz response of large number of tumor samples.

The study and characterization of cell cultures by THz technology are also worth mentioning. In ref.[178] the THz dielectric responses of living glial-like cells (PC12, SVG P12 and HMO6) have been demonstrated based on the combination of the single-interface and two-interface ATR models without cell thickness. Moreover, the glioma cells (C6 and U87) exhibited different dielectric properties compared with the glial-like cells, which could be one reason for the glioma tissue diagnosis using THz wave.

THz waves can be used to access viability of tissues

and cells. In this way, in ref.[179], an ability of TPS in the ATR configuration to evaluate (in a label-free, non-invasive, and fast manner) the effects of bioactive constituent on living glioma cells was demonstrated. Culture of glioma cells (U87) was exposed to ginsenoside Rg3. THz optical properties of cells were measured using TPS, while the cell growth inhibition rate was studied using conventional cell viability test kit or by the cellular morphological changes observed with fluorescence microscopy. The results of this study verify the TPS effectiveness in detecting the effects of glioma cells exposure to ginsenoside Rg3 (G-Rg3) *in vitro*. This highlight other important applications of THz technology in neurooncology, that is associated with assessing the efficiency of bioactive constituents and other exposure factors on living cells and tissues of the brain.

## Brain injuries

Traumatic brain injury (TBI) is the damage caused to brain by external mechanic forces, that exceeds the protective capacity of the brain and occurs due to such reasons as crush, falls, blast waves, penetration by a projectile, etc. TBI is the most common disease with high mortality and disability, while its severity is graded into mild, moderate, and severe[180]. TBI pathophysiology is complicated with diverse manifestations, including the immediate and delayed mechanisms[181]. The initial brain injury triggers a variety of molecular and biochemical events: cerebral blood flow changes, axonal shearing, metabolic imbalance, etc. The delayed secondary damage might result into neuronal and glial damage, including brain edema, neuro-inflammation, and delayed neuronal death. TBIs are responsible for 10 million deaths and hospitalizations annually. Therefore, TBI diagnosis and analysis of their severity are of crucial importance for selection of the treatment and rehabilitation strategies, as well as prognosis of the patient's survival and quality of life.

Nowadays, the advanced imaging modalities based on different physical effects are applied for the TBI diagnosis, such as computed tomography[182], diffusion tensor MRI[183], positron emission tomography[184], laser-induced photoacoustic imaging[185], fluorescence molecular imaging[186], and others. Nevertheless, all these conventional modalities of TBI diagnosis possess limited resolution, sensitivity, and specificity, as well as fail to adequately depict brain injury in mild TBI, being insensitive to diffuse axonal injuries. Hence, development of a rapid and label-free imaging technology to detect margins of TBI and distinguish between its different degrees is a challenging problem of modern neurosurgery, especially for the mild TBIs.

Most recently, THz technology was considered as an innovative tool for the intraoperative diagnosis of TBIs with different degrees. Particularly, in ref.[83], TBI models of the mild, moderate, and severe degrees in rat brains *ex vivo* were studied using TPS and THz CW imaging systems, where both freshly-excised and paraffin-embedded (dehydrated) tissues were considered. In Fig. 11(a), THz images of freshly-excised intact rat brain *ex vivo* are compared with visible and MRI images, while in Fig. 11(b), THz absorption coefficient $\alpha$ are shown for the paraffin-embedded intact rat brain and TBIs of the different degrees. The observed results revealed that THz spectroscopy and imaging of both freshly-excised and paraffin-embedded tissues allow for clear discrimination between the intact tissues and TBI, as well as between TBIs of different degrees. THz data somewhat correlate with the visible and MRI imaging. THz absorption coefficient $\alpha$ increases with the TBI degree, as compared to the intact brain. This was attributed to the edema, increased water content and decreased cell density in the injured brain. It is worth noting that the origin of contrast between TBIs and intact tissues in THz images and spectra is similar to that observed for brain tumors to some extent (Section *Tumors*).

In the followed-up ref.[84], the authors studied the intact rat brain *ex vivo* and TBI models of the different degrees using the transmission-mode 2.52 THz CW imaging. For this aim, the freshly-excised 40-μm-thick slices of brain tissues were imaged. Using the obtained data, machine learning algorithm was developed for the automatic and rapid classification between intact tissues and different degrees of TBI. Next, in ref.[187], TPS was applied for the early diagnosis of blast-induced TBI via measurements of the serum and cerebrospinal fluid. Moreover, the THz spectra of total protein in the hypothalamus and hippocampus at various time points after blast exposure were studied and analyzed, from which clear differences were observed between the THz response of an analyte at distinct time steps. Finally, the principal component analysis and machine learning algorithms were used to automatically identify the degree of blast-induced TBI. In this way, the discussed pilot research works highlight strong potential of THz spectroscopy and imaging in diagnosis of TBIs.

## Prospects and challenging problems

Despite the discussed potential applications of THz technology in different branches of neurodiagnosis, a variety of fundamental and applied problems still restrain transfer of THz technology to a medical practice. In this section, we stress the following important issues.

**THz-wave – tissue interactions & tissue heterogeneity.** In the visible and IR ranges the interactions between electromagnetic-waves and tissues have been studied comprehensively since the middle of the XX century[188]. Compared to these frequency ranges, THz biophotonics is quite novel research area, with much less data on the THz-wave – tissue interactions accumulated up to date[10,17,31]. Therefore, study of the THz optical properties of tissues, the physical effects underlying the tissue response at THz frequencies, and the origin of contrast between healthy and pathologically-altered tissues in THz range are required in order to uncover advantages of THz technology over other tools of medical spectroscopy and imaging. Particular attention must be paid to the effects of Mie scattering of THz waves on the tissue heterogeneities (Fig. 1). Namely, structural heterogeneities of intact and pathologically-altered tissues lead to the mesoscale spatial fluctuations of the THz optical properties of tissues, which gives rise to the Mie scattering of the THz waves[189,190]. These scattering effects can either hamper the THz diagnosis or provide additional useful information for the tissue quantification[41,116].

A question arises about applicability of the standard effective medium theory and the related complex dielectric permittivity models in the THz range[10,17,31]. The effective medium theory assumes tissues to be homogeneous at the THz-wavelengths scale, and, thus, it fails to account for the non-Rayleigh scattering effects. In addition to the discussed heterogeneities of rat brain tissues (Section *Brain tissue heterogeneity*), mesoscale THz-wave scatterers were observed earlier in the tissues of the human breast and tongue using the THz solid immersion microscopy[40,191]. At the same time, the effects of THz-wave scattering on such tissue heterogeneities are still to be comprehensively analyzed. Development of a correct physical model to describe the THz-wave transport in tissues with such scatterers remains an important problem of THz biophotonics. For this aim the Mie scattering theory and the radiation transfer theory can be adapted[189,190].

Heterogeneous character of tissues can complicate the intraoperative THz delineation of tumor margins. Indeed, common effective medium theory formalism involves analysis of the effective THz optical properties of tissues, which are averaged within the diffraction-limited THz beam spot and which probably would not provide reliable data for the intraoperative delineation of the tumor margins. In this way, to make the THz diagnosis possible, one should resort to novel modalities of THz spectroscopy and imaging of tissues, that overcome the Abbe diffraction limit and improve the tissue characterization[2,94]. A comprehensive analysis of the brain tissue response at THz frequencies with subwavelength spatial resolution (with an emphasis on the perifocal region of a tumor) is in order to better understand the origin of tissue heterogeneity, as well as to introduce advanced approaches for the tissue characterization and differentiation, that go far beyond a simple comparison of the effective THz optical properties of healthy and pathologically-altered tissues. In such case, being comprehensively analyzed and modeled, tissue heterogeneities can serve as a source of additional useful information for THz diagnosis.

Novel modalities of near-field THz microscopy with the resolution as high as $\sim 10^{-2}$–$10^{-4}\lambda$[94,103,104,192] can open opportunities in neurosciences and brain tumor diagnosis. Applications of the THz microscopy for detecting individual cells and their populations within the glioblastoma tissue seems to be an extremely important task that allows for solving a number of fundamental and clinical tasks. Internal heterogeneity of glioblastomas reflects the key mechanisms of their pathogenesis. Assessment of the cell-population heterogeneity allows to accurately determine the degree of biological aggressiveness of a tumor and then select the most effective way of its treatment[193,194]. Particularly, it is important to identify populations of glioma stem cells, which are able to spread widely in the brain beyond the main tumor node[195]. Glioma stem cells also form the main sources of the tumor cell mass repopulation and, thus, a key etiotropic cause of the tumor recurrence[195]. Moreover, these cells, in the form of a mesenchymal variant, provide the formation of tumor resistance to the chemotherapy and radiation therapy[196]. Detection and resection of brain tissue infiltrated with these cells is a critical task, aimed at increasing the surgical treatment radicality and improving the patient's survival. At the moment, such features of the tumor cell-population composition can be detected only by the single-cell sequencing, that remains ex-

tremely expensive and inapplicable in the intraoperative conditions[197]. The development of new tools for the intraoperative cell-population mapping in brain tissue based on the THz microscopy principles is an extremely important fundamental and clinical task.

Studying brain tissue with superresolution THz microscopy and polarization-sensitive THz imaging might be useful for understanding the course of conducting fibers (axons and their bundles) in different regions of the central nervous system. This can pave the ways for solving important problems of biomedical research, studying the connectome of various brain areas, and evaluating the functional aspects of the brain (up to the cognitoma). However, such opportunities have not been addressed yet.

**Advanced and cost-effective opto-electronic systems for the THz biophotonics.** THz instruments are still rare, cumbersome, non-ergonomic, and expensive. It will take considerable research and engineering efforts to develop portable, cost- and energy-effective THz components and systems for applications in a clinical environment. We should emphasize the need for the novel THz optical materials and related fabrication techniques, aimed at producing open-space THz optical elements[198–201], as well as hard waveguides, flexible fibers, and optical fiber bundles[5–7,202,203], aimed at the THz-wave delivery to hard-to-access tissues and internal organs for diagnostic and therapeutic applications.

We also mention the need for the THz emitters and detectors with improved performance, that can bring THz spectroscopy and imaging closer to a real-time operation, as well as improve sensitivity of THz measurements. For this aim, an increasing number of tools appear annually. Among them, we particularly mention innovative plasmonic THz photoconductive emitters and detectors[204–206], THz photoconductive antenna arrays[207], fast rotary optical delay lines[208,209] and THz devises based on novel two-dimensional semiconductors or principles of spintronics[78,210,211]. Despite a variety of superresolution near-field THz imaging modalities are vigorously explored nowadays (Section *Superresolution THz microscopy*)[2,40,41,94,103,108,109,111,113,115,116], they are still to be adapted for the needs of THz biophotonics, neuroscience, and neurodiagnosis.

**Improving the THz-wave penetration in tissues.** A limited depth of the THz-wave penetration into hydrated biological tissues (10–100 μm), considerably restrains the range of THz technology applications in biophotonics, neurosciences, and neurodiagnosis, while improvement of the THz-wave penetration depth can broaden a range of these applications. For this aim, modern methods of immersion optical clearing of tissues were recently adapted from the visible and IR ranges[188,212,213]. This method is based on the application of specific liquid chemical agents to a tissue. This leads to water diffusion from the tissues and agent diffusion into them and, thus, results in substitution of tissue water by an agent and provides temporal and reversible reduction of the tissue water content (tissue dehydration), refractive index matching, tissue shrinkage and better ordering[214]. In the visible–IR ranges, immersion optical clearing significantly suppresses the light scattering in tissues, thanks to the achievement of tissue spatial homogeneity. In turn, in the THz range, where scattering effects are not so dominating and only the tissue water strongly absorbs THz waves, the reduction of water content is more important, thus, decreasing the THz-wave absorption by tissue water and increasing the depth of THz-wave penetration into tissues[215]. In ref.[63] optimal hyperosmotic agent for the immersion optical clearing of tissues in the THz range was selected. For this aim authors measured THz absorption spectra of most common agents and estimated coefficients of their diffusion into the freshly-excised rat brain tissues. It was shown that glycerol, as an agent, provides simultaneously high penetration depth and diffusion rate. Thus, it seems to be optimal for immersion optical clearing in the THz range. In ref.[216] example of the THz-wave penetration depth enhancement were demonstrated by applying glycerol to a 224-μm-thick abdomen skin tissue *ex vivo* from a mouse. At the same time, research efforts are still required to form immersion optical clearing protocols for different branches of THz biophotonics, including the THz neurodiagnosis.

**Exogenous markers and nanoparticles for THz diagnosis.** Exogenous markers also possess high potential for THz diagnosis. Their qualitative and/or quantitative characterization can be considered as additional evaluation and connected with molecular factor for diagnosis. Most often, these markers are a complex of a specific molecule, such as an antibody or a nucleic acid fragment, or, sometimes, a metabolite, that can bind highly selectively to the desired molecular factor or accumulate specifically in pathologically-altered cells due to the peculiarities of their metabolism, and a carrier that, being accumulated in cells and tissues, can manifest itself quite

clearly when the appropriate research method is used. Today, exogenous markers are increasingly being used in neurodiagnostics involving such approaches like MRI[217,218], computed tomography[219,220], and fluorescent microscopy in visible and IR regions[221]. For example, the ingestion of 5-aminolevulinic acid results in the accumulation of protoporphyrin IX (the product of its biochemical transformation) specifically in tumor cells due to the gradient of their metabolic activity. This induces the exogenous fluorescence of the tumor and underlies the imaging approach for identification of the boundaries of brain tumor[221]. The first implementation of the same principle for THz diagnosis was described in refs.[222,223]. In particular, the use of specific nanoparticle-based biosensors[224,225] enables accurate detection of the content of various miRNAs, including miRNA-21[226]. Moreover, as it was demonstrated in ref.[227], biosensors based on gold nanoparticles can be applied for proteomic profiling, in particular, for finding molecules of epidermal growth factor receptors, as well as avidin, which plays a significant role in the pathogenesis of a number of neoplasms, including glioblastomas, and are included in clinical and diagnostic criteria. Some research also applied Gadolinium oxide as a contrast agent in THz imaging, to diminish the deteriorated imaging contrast caused by strong THz absorption by water *in vivo*[228–230].

**Multimodal diagnosis.** The combination of several diagnostic approaches, integrated together in one complex diagnostic system, possesses high efficiency in clinical practice[231]. For instance, the combination of TPI, MRI, OCT, fluorescence imaging relying on green fluorescence protein (GFP) and protoporphyrin IX (PpIX), white light imaging and H&E-stained histology make it possible to more clearly define the boundaries of brain tumors, perifocal zone, as well as to evaluate the molecular properties and the degree of pathohistological malignancy of the neoplasm[85]. In ref.[232], the application of TPS and OCT together for intraoperative neurodiagnosis offset the drawbacks of these methods; it yields differentiation of gliomas from normal tissues, performed by TPS, and discrimination between high-grade and low-grade gliomas, performed by OCT. We also should mention that not only OCT[233,234], but other methods, such as thermography[235], multi-spectral imaging[236,237], high frequency ultrasound imaging[238], Raman spectroscopy[239], polarization imaging[19,155,240] and multi-photon microscopy[241], being combined with either THz spectroscopic or imaging modalities, can be rather promising for intraoperative neurodiagnostics.

## Conclusions

In this review, modern research status in THz neurodiagnostics is discussed, including diagnosis of neurodegenerative disease, myelin deficit, tumors of the central nervous system (with an emphasis on brain gliomas), and traumatic brain injuries. Fundamental and applied challenges in study of the THz-wave – brain tissue interactions, development of THz biomedical tools and systems for neurodiagnostics, as well as strategies to accelerate their future clinical applications are also overviewed.

## References

1. Lee YS. *Principles of Terahertz Science and Technology* (Springer, New York, NY, USA, 2009).
2. Guerboukha H, Nallappan K, Skorobogatiy M. Toward real-time terahertz imaging. *Adv Opt Photonics* **10**, 843–938 (2018).
3. Yachmenev AE, Lavrukhin DV, Glinskiy IA, Zenchenko NV, Goncharov YG et al. Metallic and dielectric metasurfaces in photoconductive terahertz devices: a review. *Opt Eng* **59**, 061608 (2019).
4. Yachmenev AE, Pushkarev SS, Reznik RR, Khabibullin RA, Ponomarev DS. Arsenides-and related III-V materials-based multilayered structures for terahertz applications: various designs and growth technology. *Prog Cryst Growth Charact Mater* **66**, 100485 (2020).
5. Islam MS, Cordeiro CMB, Franco MAR, Sultana J, Cruz ALS et al. Terahertz optical fibers [invited]. *Opt Express* **28**, 16089–16117 (2020).
6. Katyba GM, Zaytsev KI, Dolganova IN, Chernomyrdin NV, Ulitko VE et al. Sapphire waveguides and fibers for terahertz applications. *Prog Cryst Growth Charact Mater* **67**, 100523 (2021).
7. Zaytsev KI, Katyba GM, Chernomyrdin NV, Dolganova IN, Kucheryavenko AS et al. Overcoming the abbe diffraction limit using a bundle of metal-coated high-refractive-index sapphire optical fibers. *Adv Opt Mater* **8**, 2000307 (2020).
8. Rubens H, Nichols EF. Heat rays of great wave length. *Phys Rev (Series I)* **4**, 314–323 (1897).
9. Auston DH. Picosecond optoelectronic switching and gating in silicon. *Appl Phys Lett* **26**, 101–103 (1975).
10. Zaytsev KI, Dolganova IN, Chernomyrdin NV, Katyba GM, Gavdush AA et al. The progress and perspectives of terahertz technology for diagnosis of neoplasms: a review. *J Opt* **22**, 013001 (2020).
11. Nikitkina AI, Bikmulina PY, Gafarova ER, Kosheleva NV, Efremov YM et al. Terahertz radiation and the skin: a review. *J Biomed Opt* **26**, 043005 (2021).
12. Lindley-Hatcher H, Stantchev RI, Chen X, Hernandez-Serrano AI, Hardwicke J et al. Real time THz imaging—opportunities and challenges for skin cancer detection. *Appl Phys Lett* **118**, 230501 (2021).
13. Reid CB, Fitzgerald A, Reese G, Goldin R, Tekkis P et al. Terahertz pulsed imaging of freshly excised human colonic

tissues. *Phys Med Biol* **56**, 4333–4353 (2011).
14. Fitzgerald AJ, Wallace VP, Pinder SE, Purushotham AD, O' Kelly P et al. Classification of terahertz-pulsed imaging data from excised breast tissue. *J Biomed Opt* **17**, 016005 (2012).
15. Ji YB, Park CH, Kim H, Kim SH, Lee GM et al. Feasibility of terahertz reflectometry for discrimination of human early gastric cancers. *Biomed Opt Express* **6**, 1398–1406 (2015).
16. Chen H, Ma SH, Yan WX, Wu XM, Wang XZ. The diagnosis of human liver cancer by using THz fiber-scanning near-field imaging. *Chin Phys Lett* **30**, 030702 (2013).
17. Smolyanskaya OA, Chernomyrdin NV, Konovko AA, Zaytsev KI, Ozheredov IA et al. Terahertz biophotonics as a tool for studies of dielectric and spectral properties of biological tissues and liquids. *Prog Quantum Electron* **62**, 1–77 (2018).
18. Shi CJ, Wu X, Peng Y. Applications of terahertz imaging technology in tumor detection. *Opto-Electronic Eng* **47**, 190638 (2020).
19. Joseph CS, Patel R, Neel VA, Giles RH, Yaroslavsky AN. Imaging of *ex vivo* nonmelanoma skin cancers in the optical and terahertz spectral regions optical and terahertz skin cancers imaging. *J Biophotonics* **7**, 295–303 (2014).
20. Yaroslavsky A, Joseph C, Patel R, Muzikansky A, Neel VA et al. Delineating nonmelanoma skin cancer margins using terahertz and optical imaging. *J Biomed Photonics Eng* **3**, 010301 (2017).
21. Pickwell E, Fitzgerald AJ, Cole BE, Taday PF, Pye RJ et al. Simulating the response of terahertz radiation to basal cell carcinoma using *ex vivo* spectroscopy measurements. *J Biomed Opt* **10**, 064021 (2005).
22. Pickwell E, Cole BE, Fitzgerald AJ, Pepper M, Wallace VP. *In vivo* study of human skin using pulsed terahertz radiation. *Phys Med Biol* **49**, 1595–1607 (2004).
23. Zaytsev KI, Gavdush AA, Chernomyrdin NV, Yurchenko SO. Highly accurate *in vivo* terahertz spectroscopy of healthy skin: variation of refractive index and absorption coefficient along the human body. *IEEE Trans Terahertz Sci Technol* **5**, 817–827 (2015).
24. Zaitsev KI, Chernomyrdin NV, Kudrin KG, Reshetov IV, Yurchenko SO. Terahertz spectroscopy of pigmentary skin nevi in vivo. *Opt Spectrosc* **119**, 404–410 (2015).
25. Zaytsev KI, Kudrin KG, Karasik VE, Reshetov IV, Yurchenko SO. *In vivo* terahertz spectroscopy of pigmentary skin nevi: pilot study of non-invasive early diagnosis of dysplasia. *Appl Phys Lett* **106**, 053702 (2015).
26. Sim YC, Park JY, Ahn KM, Park C, Son JH. Terahertz imaging of excised oral cancer at frozen temperature. *Biomed Opt Express* **4**, 1413–1421 (2013).
27. Hernandez-Cardoso GG, Amador-Medina LF, Gutierrez-Torres G, Reyes-Reyes ES, Benavides Martínez CA et al. Terahertz imaging demonstrates its diagnostic potential and reveals a relationship between cutaneous dehydration and neuropathy for diabetic foot syndrome patients. *Sci Rep* **12**, 3110 (2022).
28. Fan ST, Ung BSY, Parrott EPJ, Wallace VP, Pickwell-MacPherson E. *In vivo* terahertz reflection imaging of human scars during and after the healing process. *J Biophotonics* **10**, 1143–1151 (2017).
29. Musina GR, Chernomyrdin NV, Gafarova ER, Gavdush AA, Shpichka AJ et al. Moisture adsorption by decellularized bovine pericardium collagen matrices studied by terahertz pulsed spectroscopy and solid immersion microscopy. *Biomed Opt Express* **12**, 5368–5386 (2021).
30. Bajwa N, Au J, Jarrahy R, Sung S, Fishbein MC et al. Non-invasive terahertz imaging of tissue water content for flap viability assessment. *Biomed Opt Express* **8**, 460–474 (2017).
31. Cherkasova OP, Serdyukov DS, Nemova EF, Ratushnyak AS, Kucheryavenko AS et al. Cellular effects of terahertz waves. *J Biomed Opt* **26**, 090902 (2021).
32. DiGirolamo M, Owens JL. Water content of rat adipose tissue and isolated adipocytes in relation to cell size. *Am J Physiol* **231**, 1568–1572 (1976).
33. Ashworth PC, Pickwell-MacPherson E, Provenzano E, Pinder SE, Purushotham AD et al. Terahertz pulsed spectroscopy of freshly excised human breast cancer. *Opt Express* **17**, 12444–12454 (2009).
34. Sy S, Huang SY, Wang YXJ, Yu J, Ahuja AT et al. Terahertz spectroscopy of liver cirrhosis: investigating the origin of contrast. *Phys Med Biol* **55**, 7587–7596 (2010).
35. Oh SJ, Kim SH, Ji YB, Jeong K, Park Y et al. Study of freshly excised brain tissues using terahertz imaging. *Biomed Opt Express* **5**, 2837–2842 (2014).
36. Joseph CS, Yaroslavsky AN, Al-Arashi M, Goyette TM, Dickinson JC et al. Terahertz spectroscopy of intrinsic biomarkers for non-melanoma skin cancer. *Proc SPIE* **7215**, 72150I (2009).
37. Ney M, Abdulhalim I. Comprehensive Monte-Carlo simulator for optimization of imaging parameters for high sensitivity detection of skin cancer at the THz. *Proc SPIE* **9721**, 97210W (2016).
38. Musina GR, Nikitin PV, Chernomyrdin NV, Dolganova IN, Gavdush AA et al. Prospects of terahertz technology in diagnosis of human brain tumors – a review. *J Biomed Photonics Eng* **6**, 020201 (2020).
39. Cherkasova O, Peng Y, Konnikova M, Kistenev Y, Shi CJ et al. Diagnosis of glioma molecular markers by terahertz technologies. *Photonics* **8**, 22 (2021).
40. Chernomyrdin NV, Kucheryavenko AS, Kolontaeva GS, Katyba GM, Dolganova IN et al. Reflection-mode continuous-wave 0.15λ-resolution terahertz solid immersion microscopy of soft biological tissues. *Appl Phys Lett* **113**, 111102 (2018).
41. Chernomyrdin NV, Skorobogatiy M, Gavdush AA, Musina GR, Katyba GM et al. Quantitative super-resolution solid immersion microscopy via refractive index profile reconstruction. *Optica* **8**, 1471–1480 (2021).
42. Cole KS, Cole RH. Dispersion and absorption in dielectrics I. Alternating current characteristics. *J Chem Phys* **9**, 341–351 (1941).
43. Cole KS, Cole RH. Dispersion and absorption in dielectrics II. Direct current characteristics. *J Chem Phys* **10**, 98–105 (1942).
44. Davidson DW. Dielectric relaxation in liquids: I. The representation of relaxation behavior. *Can J Chem* **39**, 571–594 (1961).
45. Havriliak S, Negami S. A complex plane analysis of α-dispersions in some polymer systems. *J Polym Sci Part C Polym Symp* **14**, 99–117 (1966).
46. Pickwell E, Cole BE, Fitzgerald AJ, Wallace VP, Pepper M. Simulation of terahertz pulse propagation in biological systems. *Appl Phys Lett* **84**, 2190–2192 (2004).
47. Wang YF, Wang YY, Xu DG, Wu LM, Wang GQ et al. Interference elimination based on the inversion method for continuous-wave terahertz reflection imaging. *Opt Express* **28**, 21926–21939 (2020).
48. Hu BB, Nuss MC. Imaging with terahertz waves. *Opt Lett* **20**,

1716–1718 (1995).
49. Gregory IS, Tribe WR, Baker C, Cole BE, Evans MJ et al. Continuous-wave terahertz system with a 60 dB dynamic range. *Appl Phys Lett* **86**, 204104 (2005).
50. Yang X, Zhao X, Yang K, Liu YP, Liu Y et al. Biomedical applications of terahertz spectroscopy and imaging. *Trends Biotechnol* **34**, 810–824 (2016).
51. Stoik CD, Bohn MJ, Blackshire JL. Nondestructive evaluation of aircraft composites using transmissive terahertz time domain spectroscopy. *Opt Express* **16**, 17039–17051 (2008).
52. Jacobsen RH, Mittleman DM, Nuss MC. Chemical recognition of gases and gas mixtures with terahertz waves. *Opt Lett* **21**, 2011–2013 (1996).
53. Cherkasova OP, Nazarov MM, Konnikova M, Shkurinov AP. THz spectroscopy of bound water in glucose: direct measurements from crystalline to dissolved state. *J Infrared Millim Terahertz Waves* **41**, 1057–1068 (2020).
54. Komandin GA, Zaytsev KI, Dolganova IN, Nozdrin VS, Chuchupal SV et al. Quantification of solid-phase chemical reactions using the temperature-dependent terahertz pulsed spectroscopy, sum rule, and Arrhenius theory: thermal decomposition of α-lactose monohydrate. *Opt Express* **30**, 9208–9221 (2022).
55. Giuliano BM, Gavdush AA, Müller B, Zaytsev KI, Grassi T et al. Broadband spectroscopy of astrophysical ice analogues. *Astron Astrophys* **629**, A112 (2019).
56. Lucas J, Géron E, Ditchi T, Holé S. A fast fourier transform implementation of the kramers-kronig relations: application to anomalous and left handed propagation. *AIP Adv* **2**, 032144 (2012).
57. Tuchin VV, Popp J, Zakharov V. *Multimodal Optical Diagnostics of Cancer* (Springer, Cham, 2020).
58. Lee K, Jeoung K, Kim SH, Ji YB, Son H et al. Measuring water contents in animal organ tissues using terahertz spectroscopic imaging. *Biomed Opt Express* **9**, 1582–1589 (2018).
59. Png GM, Flook R, Ng BWH, Abbott D. Terahertz spectroscopy of snap-frozen human brain tissue: an initial study. *Electron Lett* **45**, 343–345 (2009).
60. Meng K, Chen TN, Chen T, Zhu LG, Liu Q et al. Terahertz pulsed spectroscopy of paraffin-embedded brain glioma. *J Biomed Opt* **19**, 077001 (2014).
61. Shi LY, Shumyatsky P, Rodríguez-Contreras A, Alfano RR. Terahertz spectroscopy of brain tissue from a mouse model of Alzheimer's disease. *J Biomed Opt* **21**, 015014 (2016).
62. Tang C, Yang J, Wang YD, Cheng J, Li XL et al. Integrating terahertz metamaterial and water nanodroplets for ultrasensitive detection of amyloid β aggregates in liquids. *Sens Actuators B Chem* **329**, 129113 (2021).
63. Musina GR, Dolganova IN, Chernomyrdin NV, Gavdush AA, Ulitko VE et al. Optimal hyperosmotic agents for tissue immersion optical clearing in terahertz biophotonics. *J Biophotonics* **13**, e202000297 (2020).
64. Gavdush AA, Chernomyrdin NV, Malakhov KM, Beshplav SIT, Dolganova IN et al. Terahertz spectroscopy of gelatin-embedded human brain gliomas of different grades: a road toward intraoperative THz diagnosis. *J Biomed Opt* **24**, 027001 (2019).
65. Gavdush AA, Chernomyrdin NV, Komandin GA, Dolganova IN, Nikitin PV et al. Terahertz dielectric spectroscopy of human brain gliomas and intact tissues *ex vivo*: double-Debye and double-overdamped-oscillator models of dielectric response. *Biomed Opt Express* **12**, 69–83 (2021).
66. Yamaguchi S, Fukushi Y, Kubota O, Itsuji T, Ouchi T et al. Brain tumor imaging of rat fresh tissue using terahertz spectroscopy. *Sci Rep* **6**, 30124 (2016).
67. Yamaguchi S, Fukushi Y, Kubota O, Itsuji T, Ouchi T et al. Origin and quantification of differences between normal and tumor tissues observed by terahertz spectroscopy. *Phys Med Biol* **61**, 6808–6820 (2016).
68. Zou Y, Li J, Cui YY, Tang PR, Du LH et al. Terahertz spectroscopic diagnosis of myelin deficit brain in mice and rhesus monkey with chemometric techniques. *Sci Rep* **7**, 5176 (2017).
69. Mu N, Yang CY, Xu DG, Wang S, Ma K et al. Molecular pathological recognition of freshly excised human glioma using terahertz ATR spectroscopy. *Biomed Opt Express* **13**, 222–236 (2022).
70. Shiraga K, Ogawa Y, Suzuki T, Kondo N, Irisawa A et al. Determination of the complex dielectric constant of an epithelial cell monolayer in the terahertz region. *Appl Phys Lett* **102**, 053702 (2013).
71. Komandin GA, Anzin VB, Ulitko VE, Gavdush AA, Mukhin AA et al. Optical cryostat with sample rotating unit for polarization-sensitive terahertz and infrared spectroscopy. *Opt Eng* **59**, 061603 (2019).
72. Nozdrin VS, Komandin GA, Spektor IE, Chernomyrdin NV, Seregin DS et al. Optical characteristics of $LaNiO_3$ thin films in the terahertz–infrared frequency range. *J Appl Phys* **131**, 025305 (2022).
73. Komandin GA, Nozdrin VS, Chernomyrdin NV, Seregin DS, Vishnevskiy AS et al. Dielectric permittivity of organosilicate glass thin films on a sapphire substrate determined using time-domain THz and Fourier IR spectroscopy. *J Phys D Appl Phys* **55**, 025303 (2022).
74. Komandin GA, Chuchupal SV, Lebedev SP, Goncharov YG, Korolev AF et al. BWO generators for terahertz dielectric measurements. *IEEE Trans Terahertz Sci Technol* **3**, 440–444 (2013).
75. Safian R, Ghazi G, Mohammadian N. Review of photomixing continuous-wave terahertz systems and current application trends in terahertz domain. *Opt Eng* **58**, 110901 (2019).
76. Mine S, Kawase K, Murate K. Real-time wide dynamic range spectrometer using a rapidly wavelength-switchable terahertz parametric source. *Opt Lett* **46**, 2618–2621 (2021).
77. Hafez HA, Kovalev S, Tielrooij KJ, Bonn M, Gensch M et al. Terahertz nonlinear optics of graphene: from saturable absorption to high-harmonics generation. *Adv Opt Mater* **8**, 1900771 (2020).
78. Burdanova MG, Tsapenko AP, Kharlamova MV, Kauppinen EI, Gorshunov BP et al. A review of the terahertz conductivity and photoconductivity of carbon nanotubes and heteronanotubes. *Adv Opt Mater* **9**, 2101042 (2021).
79. Dolganova IN, Zaytsev KI, Yurchenko SO, Karasik VE, Tuchin VV. The role of scattering in quasi-ordered structures for terahertz imaging: local order can increase an image quality. *IEEE Trans Terahertz Sci Technol* **8**, 403–409 (2018).
80. Pickwell-MacPherson E, Wallace VP. Terahertz pulsed imaging—a potential medical imaging modality. *Photodiagnosis Photodyn Ther* **6**, 128–134 (2009).
81. Darmo J, Tamosiunas V, Fasching G, Kröll J, Unterrainer K et al. Imaging with a terahertz quantum cascade laser. *Opt Express* **12**, 1879–1884 (2004).

82. Kim SM, Hatami F, Harris JS, Kurian AW, Ford J et al. Biomedical terahertz imaging with a quantum cascade laser. *Appl Phys Lett* **88**, 153903 (2006).
83. Zhao HL, Wang YY, Chen LY, Shi J, Ma K et al. High-sensitivity terahertz imaging of traumatic brain injury in a rat model. *J Biomed Opt* **23**, 036015 (2018).
84. Shi J, Wang YY, Chen TN, Xu DG, Zhao HL et al. Automatic evaluation of traumatic brain injury based on terahertz imaging with machine learning. *Opt Express* **26**, 6371–6381 (2018).
85. Ji YB, Oh SJ, Kang SG, Heo J, Kim SH et al. Terahertz reflectometry imaging for low and high grade gliomas. *Sci Rep* **6**, 36040 (2016).
86. Wu LM, Xu DG, Wang YY, Liao B, Jiang ZN et al. Study of *in vivo* brain glioma in a mouse model using continuous-wave terahertz reflection imaging. *Biomed Opt Express* **10**, 3953–3962 (2019).
87. Wang YY, Sun ZC, Xu DG, Wu LM, Chang JY et al. A hybrid method based region of interest segmentation for continuous wave terahertz imaging. *J Phys D Appl Phys* **53**, 095403 (2020).
88. Wu LM, Xu DG, Wang YY, Zhang YY, Wang HJ et al. Horizontal-scanning attenuated total reflection terahertz imaging for biological tissues. *Neurophotonics* **7**, 025005 (2020).
89. Wu LM, Wang YY, Liao B, Zhao L, Chen K et al. Temperature dependent terahertz spectroscopy and imaging of orthotopic brain gliomas in mouse models. *Biomed Opt Express* **13**, 93–104 (2022).
90. Wu LM, Xu DG, Wang YY, Ge ML, Li HB et al. Common path continuous terahertz reflection and attenuated total reflection imaging. *Acta Phys Sin* **70**, 118701 (2021).
91. Dolganova IN, Zaytsev KI, Metelkina AA, Karasik VE, Yurchenko SO. A hybrid continuous-wave terahertz imaging system. *Rev Sci Instrum* **86**, 113704 (2015).
92. Lo YH, Leonhardt R. Aspheric lenses for terahertz imaging. *Opt Express* **16**, 15991–15998 (2008).
93. Chernomyrdin NV, Frolov ME, Lebedev SP, Reshetov IV, Spektor IE et al. Wide-aperture aspherical lens for high-resolution terahertz imaging. *Rev Sci Instrum* **88**, 014703 (2017).
94. Chernomyrdin NV, Skorobogatiy M, Ponomarev DS, Bukin VV, Tuchin VV et al. Terahertz solid immersion microscopy: recent achievements and challenges. *Appl Phys Lett* **120**, 110501 (2022).
95. Ahi K. Mathematical modeling of THz point spread function and simulation of THz imaging systems. *IEEE Trans Terahertz Sci Technol* **7**, 747–754 (2017).
96. Wang Y, Qi F, Wang JK. Terahertz image super-resolution based on a complex convolutional neural network. *Opt Lett* **46**, 3123–3126 (2021).
97. McClatchey K, Reiten MT, Cheville RA. Time resolved synthetic aperture terahertz impulse imaging. *Appl Phys Lett* **79**, 4485–4487 (2001).
98. Guerboukha H, Nallappan K, Skorobogatiy M. Exploiting k-space/frequency duality toward real-time terahertz imaging. *Optica* **5**, 109–116 (2018).
99. Petrov NV, Perraud JB, Chopard A, Guillet JP, Smolyanskaya OA et al. Terahertz phase retrieval imaging in reflection. *Opt Lett* **45**, 4168–4171 (2020).
100. Heimbeck MS, Everitt HO. Terahertz digital holographic imaging. *Adv Opt Photonics* **12**, 1–59 (2020).
101. Zanotto L, Piccoli R, Dong JL, Morandotti R, Razzari L. Single-pixel terahertz imaging: a review. *Opto-Electron Adv* **3**, 200012 (2020).
102. van der Valk NCJ, Planken PCM. Electro-optic detection of subwavelength terahertz spot sizes in the near field of a metal tip. *Appl Phys Lett* **81**, 1558–1560 (2002).
103. Chen HT, Kersting R, Cho GC. Terahertz imaging with nanometer resolution. *Appl Phys Lett* **83**, 3009–3011 (2003).
104. Huber AJ, Keilmann F, Wittborn J, Aizpurua J, Hillenbrand R. Terahertz near-field nanoscopy of mobile carriers in single semiconductor nanodevices. *Nano Lett* **8**, 3766–3770 (2008).
105. Buron JD, Petersen DH, Bøggild P, Cooke DG, Hilke M et al. Graphene conductance uniformity mapping. *Nano Lett* **12**, 5074–5081 (2012).
106. Simovski CR, Belov PA, Atrashchenko AV, Kivshar YS. Wire metamaterials: physics and applications. *Adv Mater* **24**, 4229–4248 (2012).
107. Habib MS, Stefani A, Atakaramians S, Fleming SC, Argyros A et al. A prism based magnifying hyperlens with broad-band imaging. *Appl Phys Lett* **110**, 101106 (2017).
108. Schade U, Holldack K, Kuske P, Wüstefeld G, Hübers HW. THz near-field imaging employing synchrotron radiation. *Appl Phys Lett* **84**, 1422–1424 (2004).
109. Ishihara K, Ohashi K, Ikari T, Minamide H, Yokoyama H et al. Terahertz-wave near-field imaging with subwavelength resolution using surface-wave-assisted bow-tie aperture. *Appl Phys Lett* **89**, 201120 (2006).
110. Macfaden AJ, Reno JL, Brener I, Mitrofanov O. 3 $\mu$m aperture probes for near-field terahertz transmission microscopy. *Appl Phys Lett* **104**, 011110 (2014).
111. Stantchev RI, Sun BQ, Hornett SM, Hobson PA, Gibson GM et al. Noninvasive, near-field terahertz imaging of hidden objects using a single-pixel detector. *Sci Adv* **2**, e1600190 (2016).
112. Okada K, Serita K, Zang ZR, Murakami H, Kawayama I et al. Scanning laser terahertz near-field reflection imaging system. *Appl Phys Express* **12**, 122005 (2019).
113. Chernomyrdin NV, Schadko AO, Lebedev SP, Tolstoguzov VL, Kurlov VN et al. Solid immersion terahertz imaging with sub-wavelength resolution. *Appl Phys Lett* **110**, 221109 (2017).
114. Chernomyrdin NV, Zhelnov VA, Kucheryavenko AS, Dolganova IN, Katyba GM et al. Numerical analysis and experimental study of terahertz solid immersion microscopy. *Opt Eng* **59**, 061605 (2019).
115. Zhelnov VA, Zaytsev KI, Kucheryavenko AS, Katyba GM, Dolganova IN et al. Object-dependent spatial resolution of the reflection-mode terahertz solid immersion microscopy. *Opt Express* **29**, 3553–3566 (2021).
116. Kucheryavenko AS, Chernomyrdin NV, Gavdush AA, Alekseeva AI, Nikitin PV et al. Terahertz dielectric spectroscopy and solid immersion microscopy of *ex vivo* glioma model 101.8: brain tissue heterogeneity. *Biomed Opt Express* **12**, 5272–5289 (2021).
117. Wang ZB, Guo W, Li L, Luk'yanchuk B, Khan A et al. Optical virtual imaging at 50 nm lateral resolution with a white-light nanoscope. *Nat Commun* **2**, 218 (2011).
118. Upputuri PK, Pramanik M. Microsphere-aided optical microscopy and its applications for super-resolution imaging. *Opt Commun* **404**, 32–41 (2017).
119. Chen LW, Zhou Y, Li Y, Hong MH. Microsphere enhanced optical imaging and patterning: from physics to applications. *Appl Phys Rev* **6**, 021304 (2019).

120. Chen XX, Wu TL, Gong ZY, Li YC, Zhang Y et al. Sub-wavelength imaging and detection using adjustable and movable droplet microlenses. *Photonics Res* **8**, 03000225 (2020).
121. Perrin S, Donie YJ, Montgomery P, Gomard G, Lecler S. Compensated microsphere-assisted interference microscopy. *Phys Rev Appl* **13**, 014068 (2020).
122. Chen LW, Zhou Y, Wu MX, Hong MH. Remote-mode microsphere nano-imaging: new boundaries for optical microscopes. *Opto-Electron Adv* **1**, 170001 (2018).
123. Zhu YC, Chen XL, Yuan WZ, Chu ZQ, Wong KY et al. A waveguide metasurface based quasi-far-field transverse-electric superlens. *Opto-Electron Adv* **4**, 210013 (2021).
124. Geng GS, Dai GB, Li DD, Zhou SL, Li ZX et al. Imaging brain tissue slices with terahertz near-field microscopy. *Biotechnol Prog* **35**, e2741 (2019).
125. Watanabe T, Wang XQ, Tan ZG, Frahm J. Magnetic resonance imaging of brain cell water. *Sci Rep* **9**, 5084 (2019).
126. Liu GZ, Chang C, Qiao Z, Wu KJ, Zhu Z et al. Myelin sheath as a dielectric waveguide for signal propagation in the mid-infrared to terahertz spectral range. *Adv Funct Mater* **29**, 1807862 (2019).
127. Herbert E, Engel-Hills P, Hattingh C, Fouche JP, Kidd M et al. Fractional anisotropy of white matter, disability and blood iron parameters in multiple sclerosis. *Metab Brain Dis* **33**, 545–557 (2018).
128. Dong DB, Wang YL, Chang XB, Chen X, Chang X et al. Common and diagnosis-specific fractional anisotropy of white matter in schizophrenia, bipolar disorder, and major depressive disorder: evidence from comparative voxel-based meta-analysis. *Schizophr Res* **193**, 456–458 (2018).
129. Owens JA, Spitz G, Ponsford JL, Dymowski AR, Willmott C. An investigation of white matter integrity and attention deficits following traumatic brain injury. *Brain Inj* **32**, 776–783 (2018).
130. Wang J, Xu SL, Duan JJ, Yi L, Guo YF et al. Invasion of white matter tracts by glioma stem cells is regulated by a *NOTCH1–SOX2* positive-feedback loop. *Nat Neurosci* **22**, 91–105 (2019).
131. Livingston G, Sommerlad A, Orgeta V, Costafreda SG, Huntley J et al. Dementia prevention, intervention, and care. *Lancet* **390**, 2673–2734 (2017).
132. Querfurth HW, LaFerla FM. Alzheimer's disease. *N Engl J Med* **362**, 329–344 (2010).
133. Selkoe DJ, Hardy J. The amyloid hypothesis of Alzheimer's disease at 25 years. *EMBO Mol Med* **8**, 595–608 (2016).
134. Wang J, Gu BJ, Masters CL, Wang YJ. A systemic view of Alzheimer disease — insights from amyloid-β metabolism beyond the brain. *Nat Rev Neurol* **13**, 612–623 (2017).
135. Laske C, Sohrabi HR, Frost SM, López-de-Ipiña K, Garrard P et al. Innovative diagnostic tools for early detection of Alzheimer's disease. *Alzheimers Dement* **11**, 561–578 (2015).
136. Nestor PJ, Scheltens P, Hodges JR. Advances in the early detection of Alzheimer's disease. *Nat Med* **10**, S34–S41 (2004).
137. Rubinsztein DC. The roles of intracellular protein-degradation pathways in neurodegeneration. *Nature* **443**, 780–786 (2006).
138. Singh A, Kukreti R, Saso L, Kukreti S. Oxidative stress: a key modulator in neurodegenerative diseases. *Molecules* **24**, 1583 (2019).
139. Pereira TMC, Côco LZ, Ton AMM, Meyrelles SS, Campos-Toimil M et al. The emerging scenario of the gut–brain axis: the therapeutic actions of the new actor kefir against neurodegenerative diseases. *Antioxidants* **10**, 1845 (2021).
140. Lee SH, Shin S, Roh Y, Oh SJ, Lee SH et al. Label-free brain tissue imaging using large-area terahertz metamaterials. *Biosens Bioelectron* **170**, 112663 (2020).
141. Heo C, Ha T, You C, Huynh T, Lim H et al. Identifying fibrillization state of Aβ protein *via* near-field THz conductance measurement. *ACS Nano* **14**, 6548–6558 (2020).
142. Yeo WG, Gurel O, Srinivasan N, King PD, Nahar NK et al. Terahertz imaging and electromagnetic model of axon demyelination in Alzheimer's disease. *IEEE Trans Terahertz Sci Technol* **7**, 711–721 (2017).
143. Ostrom QT, Cioffi G, Gittleman H, Patil N, Waite K et al. CBTRUS statistical report: primary brain and other central nervous system tumors diagnosed in the United States in 2012–2016. *Neuro Oncol* **21**, v1–v100 (2019).
144. Wesseling P, Capper D. WHO 2016 classification of gliomas. *Neuropathol Appl Neurobiol* **44**, 139–150 (2018).
145. Brown TJ, Brennan MC, Li M, Church EW, Brandmeir NJ et al. Association of the extent of resection with survival in glioblastoma: a systematic review and meta-analysis. *JAMA Oncol* **2**, 1460–1469 (2016).
146. Louis DN, Perry A, Reifenberger G, von Deimling A, Figarella-Branger D et al. The 2016 world health organization classification of tumors of the central nervous system: a summary. *Acta Neuropathol* **131**, 803–820 (2016).
147. Rasmussen IA Jr, Lindseth F, Rygh OM, Berntsen EM, Selbekk T et al. Functional neuronavigation combined with intraoperative 3D ultrasound: Initial experiences during surgical resections close to eloquent brain areas and future directions in automatic brain shift compensation of preoperative data. *Acta Neurochir (Wien)* **149**, 365–378 (2007).
148. Senft C, Bink A, Franz K, Vatter H, Gasser T et al. Intraoperative MRI guidance and extent of resection in glioma surgery: a randomised, controlled trial. *Lancet Oncol* **12**, 997–1003 (2011).
149. Pustogarov N, Panteleev D, Goryaynov SA, Ryabova AV, Rybalkina EY et al. Hiding in the shadows: *CPOX* expression and 5-ALA induced fluorescence in human glioma cells. *Mol Neurobiol* **54**, 5699–5708 (2017).
150. Chen B, Wang HF, Ge PF, Zhao JW, Li WC et al. Gross total resection of glioma with the intraoperative fluorescence-guidance of fluorescein sodium. *Int J Med Sci* **9**, 708–714 (2012).
151. Goryaynov SA, Okhlopkov VA, Golbin DA, Chernyshov KA, Svistov DV et al. Fluorescence diagnosis in neurooncology: retrospective analysis of 653 cases. *Front Oncol* **9**, 830 (2019).
152. Kiseleva EB, Yashin KS, Moiseev AA, Timofeeva LB, Kudelkina VV et al. Optical coefficients as tools for increasing the optical coherence tomography contrast for normal brain visualization and glioblastoma detection. *Neurophotonics* **6**, 035003 (2019).
153. Dolganova IN, Aleksandrova PV, Nikitin PV, Alekseeva AI, Chernomyrdin NV et al. Capability of physically reasonable OCT-based differentiation between intact brain tissues, human brain gliomas of different WHO grades, and glioma model 101.8 from rats. *Biomed Opt Express* **11**, 6780–6798 (2020).
154. Orringer DA, Pandian B, Niknafs YS, Hollon TC, Boyle J et al. Rapid intraoperative histology of unprocessed surgical specimens via fibre-laser-based stimulated Raman scattering microscopy. *Nat Biomed Eng* **1**, 0027 (2017).
155. Feng X, Muzikansky A, Ross AH, Hamblin MR, Jermain PR et

al. Multimodal quantitative imaging of brain cancer in cultured cells. *Biomed Opt Express* **10**, 4237–4248 (2019).
156. Genina EA, Bashkatov AN, Tuchina DK, Dyachenko PA, Navolokin N et al. Optical properties of brain tissues at the different stages of glioma development in rats: pilot study. *Biomed Opt Express* **10**, 5182–5197 (2019).
157. Kircher MF, De La Zerda A, Jokerst JV, Zavaleta CL, Kempen PJ et al. A brain tumor molecular imaging strategy using a new triple-modality MRI-photoacoustic-Raman nanoparticle. *Nat Med* **18**, 829–834 (2012).
158. Fan ST, Ung B, Parrott EPJ, Pickwell-MacPherson E. Gelatin embedding: a novel way to preserve biological samples for terahertz imaging and spectroscopy. *Phys Med Biol* **60**, 2703–2713 (2015).
159. Komandin GA, Nozdrin VS, Gavdush AA, Pronin AA, Porodinkov OE et al. Effect of moisture adsorption on the broadband dielectric response of $SiO_2$-based nanoporous glass. *J Appl Phys* **126**, 224303 (2019).
160. McIntyre GI. Cell hydration as the primary factor in carcinogenesis: a unifying concept. *Med Hypotheses* **66**, 518–526 (2006).
161. Truong BCQ, Tuan HD, Wallace VP, Fitzgerald AJ, Nguyen HT. The potential of the double debye parameters to discriminate between basal cell carcinoma and normal skin. *IEEE Trans Terahertz Sci Technol* **5**, 990–998 (2015).
162. Abbas Z, Gras V, Möllenhoff K, Oros-Peusquens AM, Shah NJ. Quantitative water content mapping at clinically relevant field strengths: a comparative study at 1.5T and 3T. *NeuroImage* **106**, 404–413 (2015).
163. Neeb H, Zilles K, Shah NJ. A new method for fast quantitative mapping of absolute water content in vivo. *NeuroImage* **31**, 1156–1168 (2006).
164. Neeb H, Ermer V, Stocker T, Shah NJ. Fast quantitative mapping of absolute water content with full brain coverage. *NeuroImage* **42**, 1094–1109 (2008).
165. DiResta GR, Lee J, Arbit E. Measurement of brain tissue specific gravity using pycnometry. *J Neurosci Methods* **39**, 245–251 (1991).
166. Menon SS, Guruvayoorappan C, Sakthivel KM, Rasmi RR. Ki-67 protein as a tumour proliferation marker. *Clin Chim Acta* **491**, 39–45 (2019).
167. Sobecki M, Mrouj K, Camasses A, Parisis N, Nicolas E et al. The cell proliferation antigen Ki-67 organises heterochromatin. *eLife* **5**, e13722 (2016).
168. Wong E, Nahar N, Hau E, Varikatt W, Gebski V et al. Cut-point for Ki-67 proliferation index as a prognostic marker for glioblastoma. *Asia Pac J Clin Oncol* **15**, 5–9 (2019).
169. Henker C, Kriesen T, Schneider B, Glass Ä, Scherer M et al. Correlation of Ki-67 index with volumetric segmentation and its value as a prognostic marker in glioblastoma. *World Neurosurg* **125**, e1093–e1103 (2019).
170. Stine ZE, Walton ZE, Altman BJ, Hsieh AL, Dang CV. MYC, metabolism, and cancer. *Cancer Discov* **5**, 1024–1039 (2015).
171. Turkalp Z, Karamchandani J, Das S. *IDH* mutation in glioma: new insights and promises for the future. *JAMA Neurol* **71**, 1319–1325 (2014).
172. Ceccarelli M, Barthel FP, Malta TM, Sabedot TS, Salama SR et al. Molecular profiling reveals biologically discrete subsets and pathways of progression in diffuse glioma. *Cell* **164**, 550–563 (2016).
173. Bell EH, Zhang PX, Fisher BJ, Macdonald DR, McElroy JP et al. Association of *MGMT* promoter methylation status with survival outcomes in patients with high-risk glioma treated with radiotherapy and temozolomide: an analysis from the NRG oncology/RTOG 0424 trial. *JAMA Oncol* **4**, 1405–1409 (2018).
174. Sasaki T, Kinoshita M, Fujita K, Fukai J, Hayashi N et al. Radiomics and *MGMT* promoter methylation for prognostication of newly diagnosed glioblastoma. *Sci Rep* **9**, 14435 (2019).
175. Chen WQ, Peng Y, Jiang XK, Zhao JY, Zhao HW et al. Isomers identification of 2-hydroxyglutarate acid disodium salt (2HG) by terahertz time-domain spectroscopy. *Sci Rep* **7**, 12166 (2017).
176. Fedoseeva VV, Postovalova EA, Khalansky AS, Razzhivina VA, Gelperina SE et al. Drug-induced pathomorphosis of glioblastoma 101.8 in wistar rats treated with doxorubicin bound to poly (lactide-co-glycolide) nanoparticles. *Sovrem Tekhnologii Med* **10**, 105 (2018).
177. Chernomyrdin NV, Gavdush AA, Beshplav SIT, Malakhov KM, Kucheryavenko AS et al. *In vitro* terahertz spectroscopy of gelatin-embedded human brain tumors: a pilot study. *Proc SPIE* **10716**, 107160S (2018).
178. Wang YY, Jiang ZN, Xu DG, Chen TN, Chen BK et al. Study of the dielectric characteristics of living glial-like cells using terahertz ATR spectroscopy. *Biomed Opt Express* **10**, 5351–5361 (2019).
179. Liao YS, Zhang MK, Tang MJ, Chen LG, Li XQ et al. Label-free study on the effect of a bioactive constituent on glioma cells *in vitro* using terahertz ATR spectroscopy. *Biomed Opt Express* **13**, 2380–2392 (2022).
180. Ghajar J. Traumatic brain injury. *Lancet* **356**, 923–929 (2000).
181. Shlosberg D, Benifla M, Kaufer D, Friedman A. Blood–brain barrier breakdown as a therapeutic target in traumatic brain injury. *Nat Rev Neurol* **6**, 393–403 (2010).
182. Shenton ME, Hamoda HM, Schneiderman JS, Bouix S, Pasternak O et al. A review of magnetic resonance imaging and diffusion tensor imaging findings in mild traumatic brain injury. *Brain Imaging Behav* **6**, 137–192 (2012).
183. Wunder A, Schoknecht K, Stanimirovic DB, Prager O, Chassidim Y. Imaging blood-brain barrier dysfunction in animal disease models. *Epilepsia* **53**, 14–21 (2012).
184. Coles JP, Fryer TD, Smielewski P, Rice K, Clark JC et al. Defining ischemic burden after traumatic brain injury using $^{15}O$ PET imaging of cerebral physiology. *J Cereb Blood Flow Metab* **24**, 191–201 (2004).
185. Yang SH, Xing D, Lao YQ, Yang DW, Zeng LM et al. Noninvasive monitoring of traumatic brain injury and post-traumatic rehabilitation with laser-induced photoacoustic imaging. *Appl Phys Lett* **90**, 243902 (2007).
186. Zhang XD, Wang HS, Antaris AL, Li LL, Diao S et al. Traumatic brain injury imaging in the second near-infrared window with a molecular fluorophore. *Adv Mater* **28**, 6872–6879 (2016).
187. Wang YY, Wang GQ, Xu DG, Jiang BZ, Ge ML et al. Terahertz spectroscopic diagnosis of early blast-induced traumatic brain injury in rats. *Biomed Opt Express* **11**, 4085–4098 (2020).
188. Bashkatov AN, Berezin KV, Dvoretskiy KN, Chernavina ML, Genina EA et al. Measurement of tissue optical properties in the context of tissue optical clearing. *J Biomed Opt* **23**, 091416 (2018).
189. Tuchin VV. *Tissue Optics: Light Scattering Methods and Instruments for Medical Diagnostics* 3rd ed (SPIE Press, Bellingham,

Washington, USA, 2015).
190. Ishimaru A. *Electromagnetic Wave Propagation, Radiation, and Scattering: From Fundamentals to Applications* (Wiley-IEEE Press, Hoboken, New Jersey, USA, 2017).
191. Chernomyrdin NV, Kucheryavenko AS, Rimskaya EN, Dolganova IN, Zhelnov VA et al. Terahertz microscope based on solid immersion effect for imaging of biological tissues. *Opt Spectrosc* **126**, 560–567 (2019).
192. Li ZX, Yan SH, Zang ZY, Geng GS, Yang ZB et al. Single cell imaging with near-field terahertz scanning microscopy. *Cell Prolif* **53**, e12788 (2020).
193. Neftel C, Laffy J, Filbin MG, Hara T, Shore ME et al. An integrative model of cellular states, plasticity, and genetics for glioblastoma. *Cell* **178**, 835–849.e21 (2019).
194. Dirkse A, Golebiewska A, Buder T, Nazarov PV, Muller A et al. Stem cell-associated heterogeneity in Glioblastoma results from intrinsic tumor plasticity shaped by the microenvironment. *Nat Commun* **10**, 1787 (2019).
195. Zhou D, Alver BM, Li S, Hlady RA, Thompson JJ et al. Distinctive epigenomes characterize glioma stem cells and their response to differentiation cues. *Genome Biol* **19**, 43 (2018).
196. Behnan J, Finocchiaro G, Hanna G. The landscape of the mesenchymal signature in brain tumours. *Brain* **142**, 847–866 (2019).
197. Ren XW, Kang BX, Zhang ZM. Understanding tumor ecosystems by single-cell sequencing: promises and limitations. *Genome Biol* **19**, 211 (2018).
198. Guerboukha H, Nallappan K, Cao Y, Seghilani M, Azaña J et al. Planar porous components for low-loss terahertz optics. *Adv Opt Mater* **7**, 1900236 (2019).
199. Ulitko VE, Zotov AK, Gavdush AA, Katyba GM, Komandin GA et al. Nanoporous $SiO_2$ based on annealed artificial opals as a favorable material platform of terahertz optics. *Opt Mater Express* **10**, 2100–2113 (2020).
200. Ulitko VE, Katyba GM, Zhelnov VA, Shmytko IM, Emelchenko GA et al. Opal-based terahertz optical elements fabricated by self-assembly of porous $SiO_2$ nanoparticles. *Opt Express* **29**, 13764–13777 (2021).
201. Li JT, Wang GC, Yue Z, Liu JY, Li J et al. Dynamic phase assembled terahertz metalens for reversible conversion between linear polarization and arbitrary circular polarization. *Opto-Electron Adv* **5**, 210062 (2022).
202. Katyba GM, Chizhov PA, Kurlov VN, Dolganova IN, Garnov SV et al. THz generation by two-color laser air plasma coupled to antiresonance hollow-core sapphire waveguides: THz-wave delivery and angular distribution management. *Opt Express* **30**, 4215–4230 (2022).
203. Katyba GM, Zaytsev KI, Chernomyrdin NV, Shikunova IA, Komandin GA et al. Sapphire photonic crystal waveguides for terahertz sensing in aggressive environments. *Adv Opt Mater* **6**, 1800573 (2018).
204. Ponomarev DS, Lavrukhin DV, Zenchenko NV, Frolov TV, Glinskiy IA et al. Boosting photoconductive large-area THz emitter via optical light confinement behind a highly refractive sapphire-fiber lens. *Opt Lett* **47**, 1899–1902 (2022).
205. Lepeshov S, Gorodetsky A, Krasnok A, Rafailov E, Belov P. Enhancement of terahertz photoconductive antenna operation by optical nanoantennas. *Laser Photon Rev* **11**, 1600199 (2017).
206. Lavrukhin DV, Yachmenev AE, Glinskiy IA, Khabibullin RA, Goncharov YG et al. Terahertz photoconductive emitter with dielectric-embedded high-aspect-ratio plasmonic grating for operation with low-power optical pumps. *AIP Adv* **9**, 015112 (2019).
207. Henri R, Nallappan K, Ponomarev DS, Guerboukha H, Lavrukhin DV et al. Fabrication and characterization of an 8 × 8 terahertz photoconductive antenna array for spatially resolved time domain spectroscopy and imaging applications. *IEEE Access* **9**, 117691–117702 (2021).
208. Guerboukha H, Markov A, Qu H, Skorobogatiy M. Time resolved dynamic measurements at THz frequencies using a rotary optical delay line. *IEEE Trans Terahertz Sci Technol* **5**, 564–572 (2015).
209. Skorobogatiy M. Linear rotary optical delay lines. *Opt Express* **22**, 11812–11833 (2014).
210. Ryzhii V, Otsuji T, Shur M. Graphene based plasma-wave devices for terahertz applications. *Appl Phys Lett* **116**, 140501 (2020).
211. Tong MY, Hu YZ, Xie XN, Zhu XG, Wang ZY et al. Helicity-dependent THz emission induced by ultrafast spin photocurrent in nodal-line semimetal candidate $Mg_3Bi_2$. *Opto-Electron Adv* **3**, 200023 (2020).
212. Lazareva EN, Oliveira L, Yanina IY, Chernomyrdin NV, Musina GR et al. Refractive index measurements of tissue and blood components and OCAs in a wide spectral range. In *Handbook of Tissue Optical Clearing: New Prospects in Optical Imaging* (eds. Tuchin VV, Zhu D, Genina EA) 141–166 (CRC Press, Boca Raton, FL, USA, 2022).
213. Smolyanskaya OA, Zaytsev KI, Dolganova IN, Musina GR, Tuchina DK et al. Tissue optical clearing in the terahertz range. In *Handbook of Tissue Optical Clearing: New Prospects in Optical Imaging* (eds. Tuchin VV, Zhu D, Genina EA) 445–458 (CRC Press, Boca Raton, FL, USA, 2022).
214. Tuchin VV, Zhu D, Genina EA. *Handbook of Tissue Optical Clearing: New Prospects in Optical Imaging* (CRC Press, Boca Raton, FL USA, 2022).
215. Musina GR, Gavdush AA, Chernomyrdin NV, Dolganova IN, Ulitko VE et al. Optical properties of hyperosmotic agents for immersion clearing of tissues in terahertz spectroscopy. *Opt Spectrosc* **128**, 1026–1035 (2020).
216. Oh SJ, Kim SH, Jeong K, Park Y, Huh YM et al. Measurement depth enhancement in terahertz imaging of biological tissues. *Opt Express* **21**, 21299–21305 (2013).
217. Xiao YD, Paudel R, Liu J, Ma C, Zhang ZS et al. MRI contrast agents: classification and application (review). *Int J Mol Med* **38**, 1319–1326 (2016).
218. Faucher L, Tremblay M, Lagueux J, Gossuin Y, Fortin MA. Rapid synthesis of PEGylated ultrasmall gadolinium oxide nanoparticles for cell labeling and tracking with MRI. *ACS Appl Mater Interfaces* **4**, 4506–4515 (2012).
219. Rutten A, Prokop M. Contrast agents in X-ray computed tomography and its applications in oncology. *Anticancer Agents Med Chem* **7**, 307–316 (2007).
220. Xu XY, Liu K, Wang Y, Zhang CC, Shi MH et al. A multifunctional low-generation dendrimer-based nanoprobe for the targeted dual mode MR/CT imaging of orthotopic brain gliomas. *J Mater Chem B* **7**, 3639–3643 (2019).
221. Mahmoudi K, Garvey KL, Bouras A, Cramer G, Stepp H et al. 5-aminolevulinic acid photodynamic therapy for the treatment of high-grade gliomas. *J Neurooncol* **141**, 595–607 (2019).

222. Xu WD, Xie LJ, Zhu JF, Xu X, Ye ZZ et al. Gold nanoparticle-based terahertz metamaterial sensors: mechanisms and applications. *ACS Photonics* **3**, 2308–2314 (2016).
223. RoyChoudhury S, Rawat V, Jalal AH, Kale SN, Bhansali S. Recent advances in metamaterial split-ring-resonator circuits as biosensors and therapeutic agents. *Biosens Bioelectron* **86**, 595–608 (2016).
224. Peng Y, Shi CJ, Wu X, Zhu YM, Zhuang SL. Terahertz imaging and spectroscopy in cancer diagnostics: a technical review. *BME Front* **2020**, 2547609 (2020).
225. Peng Y, Shi CJ, Zhu YM, Gu M, Zhuang SL. Terahertz spectroscopy in biomedical field: a review on signal-to-noise ratio improvement. *PhotoniX* **1**, 12 (2020).
226. Yang K, Li JN, Lamy de la Chapelle M, Huang GR, Wang YX et al. A terahertz metamaterial biosensor for sensitive detection of microRNAs based on gold-nanoparticles and strand displacement amplification. *Biosens Bioelectron* **175**, 112874 (2021).
227. Liu K, Zhang R, Liu Y, Chen XQ, Li KD et al. Gold nanoparticle enhanced detection of EGFR with a terahertz metamaterial biosensor. *Biomed Opt Express* **12**, 1559–1567 (2021).
228. Yan ZY, Zhu LG, Meng K, Huang WX, Shi QW. THz medical imaging: from *in vitro* to *in vivo*. *Trends Biotechnol* **40**, 816–830 (2022).
229. Huang QQ, Zou Y, Zhong SC, Yang X, Li J et al. Silica-coated gold nanorods with high photothermal efficiency and biocompatibility as a contrast agent for *in vitro* terahertz imaging. *J Biomed Nanotechnol* **15**, 910–920 (2019).
230. Cristian CR, Thomas S, Vasile D, Stanciu GD, Alexa-Stratulat T et al. Research on functionalized gadolinium oxide nanoparticles for MRI and THz imaging. In *2018 International Conference and Exposition on Electrical And Power Engineering (EPE)* 646–649 (IEEE, 2018); http://doi.org/10.1109/ICEPE.2018.8559855.
231. Smolyanskaya OA, Lazareva EN, Nalegaev SS, Petrov NV, Zaytsev KI et al. Multimodal optical diagnostics of glycated biological tissues. *Biochemistry (Mosc)* **84**, 124–143 (2019).
232. Chernomyrdin NV, Dolganova IN, Beshplav SIT, Aleksandrova PV, Musina GR et al. Differentiation of healthy and malignant brain tissues using terahertz pulsed spectroscopy and optical coherence tomography. *Proc SPIE* **10864**, 1086406 (2019).
233. Huang D, Swanson EA, Lin CP, Schuman JS, Stinson WG et al. Optical coherence tomography. *Science* **254**, 1178–1181 (1991).
234. Patel R, Khan A, Quinlan R, Yaroslavsky AN. Polarization-sensitive multimodal imaging for detecting breast cancer. *Cancer Res* **74**, 4685–4693 (2014).
235. Jones BF. A reappraisal of the use of infrared thermal image analysis in medicine. *IEEE Trans Med Imaging* **17**, 1019–1027 (1998).
236. Chernomyrdin NV, Lesnichaya AD, Yakovlev EV, Kudrin KG, Cherkasova OP et al. Differentiation of basal cell carcinoma and healthy skin using multispectral modulation autofluorescence imaging: a pilot study. *J Biomed Photonics Eng* **5**, 010302 (2019).
237. Stenquist B, Ericson MB, Strandeberg C, Mölne L, Rosén A et al. Bispectral fluorescence imaging of aggressive basal cell carcinoma combined with histopathological mapping: a preliminary study indicating a possible adjunct to Mohs micrographic surgery. *Br J Dermatol* **154**, 305–309 (2006).
238. Kleinerman R, Whang TB, Bard RL, Marmur ES. Ultrasound in dermatology: Principles and applications. *J Am Acad Dermatol* **67**, 478–487 (2012).
239. Lui H, Zhao JH, McLean D, Zeng HS. Real-time Raman spectroscopy for *in vivo* skin cancer diagnosis. *Cancer Res* **72**, 2491–2500 (2012).
240. Fan B, Neel VA, Yaroslavsky AN. Multimodal imaging for non-melanoma skin cancer margin delineation. *Lasers Surg Med* **49**, 319–326 (2017).
241. Paoli J, Smedh M, Wennberg AM, Ericson MB. Multiphoton laser scanning microscopy on non-melanoma skin cancer: morphologic features for future non-invasive diagnostics. *J Invest Dermatol* **128**, 1248–1255 (2008).

## Acknowledgements

The work was supported by the Russian Science Foundation, Project # 22-22-00596.

## Author contributions

KIZ and NVC were responsible for the text of the paper; GRM made overview of the references and arranged figures; PVN provided biomedical interpretations; IND, ASK, AIA, YW, DX, QS and VVT took part in discussions.

## Competing interests

The authors declare no competing financial interests.